

Regularized Calibration with Successive Rounding for Post-Training Quantization

Seohyeon Cha¹ Huancheng Chen¹ Dongjun Kim¹ Haoran Zhang¹
 Kevin Chan² Gustavo de Veciana¹ Haris Vikalo¹

Abstract

Large language models (LLMs) deliver robust performance across diverse applications, yet their deployment often faces challenges due to the memory and latency costs of storing and accessing billions of parameters. Post-training quantization (PTQ) enables efficient inference by mapping pretrained weights to low-bit formats without retraining, but its effectiveness depends critically on both the quantization objective and the rounding procedure used to obtain low-bit weight representations. In this work, we show that interpolating between symmetric and asymmetric calibration acts as a form of regularization that preserves the standard quadratic structure used in PTQ while providing robustness to activation mismatch. Building on this perspective, we derive a simple successive rounding procedure that naturally incorporates asymmetric calibration, as well as a bounded-search extension that allows for an explicit trade-off between quantization quality and the compute cost. Experiments across multiple LLM families, quantization bit-widths, and benchmarks demonstrate that the proposed bounded search based on a regularized asymmetric calibration objective consistently improves perplexity and accuracy over PTQ baselines, while incurring only modest and controllable additional computational cost. Code is available at [GitHub](#).

1. Introduction

Large language models (LLMs) have demonstrated remarkable performance across a wide range of tasks and application domains, but their size presents a major challenge to practical deployment (Ge et al., 2023; Yang et al., 2024;

¹Department of Electrical and Computer Engineering, The University of Texas at Austin, TX, USA. ²DEVCOM Army Research Laboratory, Adelphi, MD, USA. Correspondence to: Seohyeon Cha <seohyeon.cha@utexas.edu>.

Nam et al., 2024). Modern transformer-based LLMs contain billions of parameters, which translates to tens to hundreds of gigabytes of weights in standard floating-point formats and substantial inference latency due to memory traffic (Gholami et al., 2024; Kim et al., 2023). These costs limit deployment on commodity hardware and make on-device or edge inference largely impractical (Xu et al., 2024). As a result, improving inference efficiency by reducing both memory footprint and runtime while preserving accuracy has become a central challenge in bringing LLM capabilities to real-world systems.

Post-training quantization (PTQ) enables compression of a pretrained model without retraining by mapping its weights to low-bit integer formats, thus providing a practical path to efficient inference. To remain scalable, PTQ is typically implemented as a layer-wise optimization procedure: a small calibration set is used to define a local reconstruction objective that quantifies the mismatch between quantized and full-precision layer outputs, and the quantized weights are obtained by approximately solving a discrete rounding problem over a low-bit grid (Nagel et al., 2020; Hubara et al., 2021; Li et al., 2021; Frantar & Alistarh, 2022; Frantar et al., 2022). This formulation highlights two closely related design choices that ultimately govern the performance of a quantized model: (i) the choice of the layer-wise calibration objective, and (ii) the rounding procedure used to navigate the resulting discrete search space.

A common layer-wise objective in PTQ adopts a Hessian-based *symmetric* formulation, in which reconstruction error is evaluated using activations generated by previously quantized layers (Nagel et al., 2020). This choice is computationally convenient because it relies only on layer-local calibration statistics, rather than requiring end-to-end optimization across layers. However, it is inherently local: errors introduced by early quantization decisions can propagate through subsequent layers and distort intermediate activations (Ding et al., 2023). To address this concern, several recent methods adopt an *asymmetric* calibration objective that matches quantized layer outputs to the corresponding full-precision outputs, thus helping reduce error accumulation during calibration (Li et al., 2025; Liao et al.,

2024). Concretely, these methods compare the layer output under inputs produced by full-precision preceding layers to the layer output under inputs produced by the already-quantized preceding layers. Orthogonal lines of work focus on strengthening the reconstruction proxy itself, either by incorporating more informative curvature approximations (Kim et al., 2025; Tseng et al., 2025; Kim et al., 2024) or by relaxing layer-wise independence and considering cross-block reconstruction error (Ding et al., 2023).

Even with a well-chosen calibration objective, PTQ ultimately requires solving a *discrete* optimization problem over low-bit weight grids. Most existing methods obtain quantized weights via sequential rounding of the weight matrix, either through greedy column-wise rounding (Frantar et al., 2022; Chee et al., 2023; Chen et al., 2025; Zheng et al., 2025) or using iterative refinement schemes such as coordinate descent (Behdin et al., 2023; Nair & Suggala, 2024). Because these solvers make local decisions at each step, the choice of rounding strategy directly affects quantization performance: suboptimal early decisions can propagate across weight columns and lead to substantial degradation in reconstruction quality.

In this work, we develop a PTQ framework that jointly improves the layer-wise calibration objective and the rounding procedure used to obtain quantized weights. On the objective side, we introduce an interpolation mechanism that regularizes full-precision and quantized activations, yielding an asymmetry-controlled calibration proxy governed by a single parameter. We show that this proxy admits a decomposition into a standard symmetric reconstruction term plus an asymmetric regularizer, providing a direct and interpretable mechanism for controlling its strength. On the algorithmic side, we show that the resulting regularized objective induces a discrete optimization problem that can be solved efficiently via sequential rounding. This formulation leads to a simple greedy rounding procedure, as well as a bounded-search extension that explores multiple partial assignments and enables an explicit trade-off between quantization quality and computational cost. Our contributions are summarized as follows:

- **Regularized Asymmetric Calibration.** We show that interpolating between symmetric and asymmetric calibration admits an *exact* decomposition into a standard symmetric reconstruction objective plus an explicit asymmetric regularizer. This provides a clear and interpretable mechanism for controlling the strength of asymmetry in post-training quantization while preserving the quadratic structure required for efficient optimization.
- **Search-Enhanced Sequential Rounding.** We show that the resulting regularized objective induces a discrete optimization problem that can be efficiently solved using sequential rounding. This leads to a simple greedy rounding algorithm, as well as a bounded-search extension that

improves quantization quality over greedy rounding and allows an explicit trade-off between computational cost and reconstruction error.

- **Empirical Evaluation.** Through comprehensive experiments across multiple LLMs, quantization bit-widths, and benchmarks, we demonstrate that combining regularized asymmetric calibration with search-enhanced sequential rounding consistently achieves improved perplexity and downstream accuracy at modest additional compute cost.

2. Background

2.1. Layer-wise PTQ as Quadratic Proxy Minimization

We consider post-training quantization (PTQ) of a single linear module (e.g., attention or MLP) within a pretrained transformer with L layers. For each layer $l \in \{1, \dots, L\}$, let $W^l \in \mathbb{R}^{m \times n}$ denote the full-precision weight matrix and \hat{W}^l its quantized counterpart. Most PTQ methods proceed *layer-wise*: when quantizing layer l , we form a calibration set of inputs $(x_t^l)_{t=1}^N \subset \mathbb{R}^n$, where each x_t^l is the activation fed into layer l obtained by running the calibration sequence through the preceding quantized layers $(\hat{W}^{l'})_{l' < l}$. Stacking these activations as columns, $X^l := [x_1^l, \dots, x_N^l] \in \mathbb{R}^{n \times N}$, the standard symmetric reconstruction loss is

$$\mathcal{L}_{\text{sym}}(\hat{W}^l; X^l) := \|(W^l - \hat{W}^l)X^l\|_F^2 \quad (1)$$

$$= \text{tr}((W^l - \hat{W}^l)H^l(W^l - \hat{W}^l)^\top), \quad (2)$$

where $H^l := X^l X^{l\top} \in \mathbb{R}^{n \times n}$ denotes the Hessian matrix.

Many PTQ solvers, such as GPTQ, minimize (1) using sequential or coordinate-wise rounding guided by curvature information derived from the Hessian or its approximations (Frantar et al., 2022). Recent work further improves this quadratic proxy by refining curvature estimates beyond simple second moments (Kim et al., 2025; Tseng et al., 2025).

2.2. Asymmetric Calibration

In layer-wise PTQ, once earlier layers have been quantized, the inputs to a later layer are no longer the same as those produced by the original full-precision network. For a fixed layer l , we distinguish between *student* and *teacher* calibration inputs. Let $X_q^l \in \mathbb{R}^{n \times N}$ denote the activations feeding into layer l when the preceding layers use quantized weights $(\hat{W}^{l'})_{l' < l}$ (student), and let $X_f^l \in \mathbb{R}^{n \times N}$ denote the corresponding activations when the same preceding layers use full-precision weights $(W^{l'})_{l' < l}$ (teacher). The t -th columns $x_{q,t}^l$ and $x_{f,t}^l$ correspond to the same calibration token, but generally satisfy $x_{q,t}^l \neq x_{f,t}^l$ due to accumulated upstream quantization error.

The symmetric loss (1) implicitly assumes that the quantized layer should match full-precision weights when evaluated on *student* activations X_q^l . However, X_q^l can deviate from

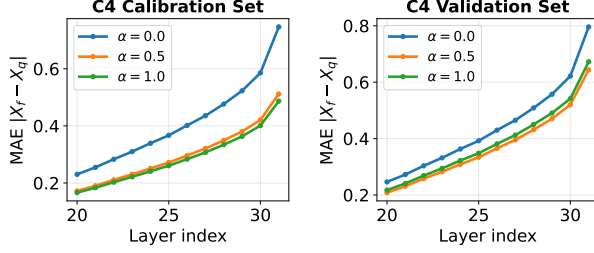


Figure 1. Mean activation error (MAE) $|X_f - X_q|$ across transformer layers of L2-7B on C4, evaluated on the calibration set (left) and a validation set (right) under greedy layer-wise rounding. Although $\alpha = 1$ achieves the lowest calibration error, intermediate values of α reduce error on the validation set.

the corresponding full-precision activations X_f^l , and this representation mismatch may propagate to later layers. To explicitly account for this effect, GPTAQ (Li et al., 2025) introduces an *asymmetric* calibration objective that measures the output discrepancy between the full-precision layer evaluated on X_f^l and the quantized layer evaluated on X_q^l :

$$\mathcal{L}_{\text{asym}}(\hat{W}^l; X_f^l, X_q^l) := \|\boldsymbol{W}^l X_f^l - \hat{W}^l X_q^l\|_F^2. \quad (3)$$

This objective directly captures the representation mismatch induced by upstream quantization. In the following, we omit the layer index l for notational simplicity.

3. Regularized Calibration for Quantization

One challenge in PTQ is designing a calibration objective that generalizes beyond the calibration set. Symmetric objectives are computationally convenient but can exacerbate error propagation by fitting to quantized activations, while fully asymmetric matching directly targets full-precision behavior but can become overly sensitive to activation mismatches caused by upstream quantization.

To interpolate between these two regimes, we introduce a parameter $\alpha \in [0, 1]$ and define the α -weighted activation

$$X_\alpha = \alpha X_f + (1 - \alpha) X_q \in \mathbb{R}^{n \times N}. \quad (4)$$

We then optimize the weighted asymmetric proxy

$$\mathcal{L}(\hat{W}; \alpha) = \|WX_\alpha - \hat{W}X_q\|_F^2. \quad (5)$$

At $\alpha = 0$, this objective reduces to the standard symmetric reconstruction loss, which corresponds to the usual second-order weight perturbation proxy. At $\alpha = 1$, it becomes the pure teacher–student matching objective.

Empirically, we observe that the best performance is typically achieved at an intermediate value of α rather than at the endpoints $\alpha \in \{0, 1\}$. Figure 1 illustrates this behavior: while $\alpha = 1$ can reduce mismatch on the calibration set, it does not necessarily yield the lowest mismatch on

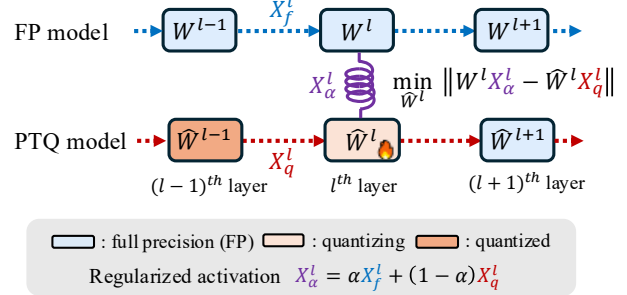


Figure 2. Regularized layer-wise calibration using interpolated activations $X_\alpha^l = \alpha X_f^l + (1 - \alpha) X_q^l$ that blend full precision and quantized features during weight optimization at layer l .

held-out validation features, whereas intermediate values of α improve validation performance. This behavior suggests that controlled asymmetry acts as an implicit regularizer by mitigating overfitting to calibration features. We formalize this interpretation next.

3.1. Asymmetric Loss as Regularization

Here we show that the interpolated proxy admits a decomposition into a standard symmetric reconstruction term and an asymmetric teacher–student term, allowing asymmetry to be an explicit regularization of the symmetric objective.

Proposition 3.1 (Decomposition of the interpolated proxy). *For any $\alpha \in [0, 1]$, the interpolated proxy $\mathcal{L}(\hat{W}; \alpha)$ admits the decomposition*

$$\mathcal{L}(\hat{W}; \alpha) \equiv \alpha \mathcal{L}_{asym}(\hat{W}) + (1 - \alpha) \mathcal{L}_{sym}(\hat{W}), \quad (6)$$

where \equiv denotes equality up to an additive constant independent of \hat{W} .

The proof is given in Section B.1. Hence, for any $\alpha \in [0, 1)$, minimizing (5) is equivalent to

$$\min_{\hat{W}} \mathcal{L}_{\text{sym}}(\hat{W}) + \gamma(\alpha) \mathcal{L}_{\text{asym}}(\hat{W}), \quad \gamma(\alpha) := \frac{\alpha}{1-\alpha}. \quad (7)$$

Under this view, \mathcal{L}_{sym} serves as the base proxy, while $\mathcal{L}_{\text{asym}}$ acts as an explicit regularizer that biases the solution toward agreement with teacher-side features X_f . Consequently, performance depends critically on selecting α to balance the base proxy and the teacher-alignment regularization, which motivates the principled α -choice strategies.

3.2. Regularization Parameter Selection for PTQ

We present two practical mechanisms: (i) a closed-form, module-wise update, and (ii) a stochastic sampling rule, which we use as our primary choice in practice.

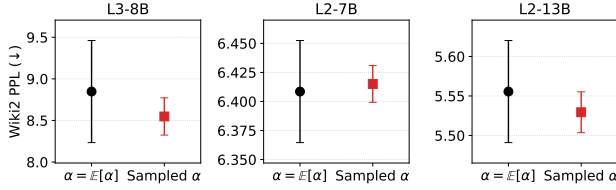


Figure 3. Mean Wiki2 perplexity (\pm std. over 5 seeds) for a fixed $\alpha = \mathbb{E}[\alpha]$ vs. sampled α . Sampling reduces variability across runs and achieves equal or lower mean perplexity across all models.

3.2.1. CLOSED-FORM UPDATE

For a fixed quantized candidate \hat{W} , $\mathcal{L}(\hat{W}, \alpha)$ depends on α only through the α -weighted activations X_α , and admits a closed-form minimizer. Let $U := W(X_f - X_q)$. Then the minimizer of $\alpha \mapsto \mathcal{L}(\hat{W}, \alpha)$ over $[0, 1]$ is given as follows.

Proposition 3.2 (Optimal α). *Fix any $\hat{W} \in \mathcal{Q}$. If $U \neq 0$, then the unique minimizer of $\alpha \mapsto \mathcal{L}(\hat{W}, \alpha)$ over $[0, 1]$ is*

$$\alpha^*(\hat{W}) = \Pi_{[0,1]} \left(-\frac{\langle (W - \hat{W})X_q, U \rangle_F}{\|U\|_F^2} \right), \quad (8)$$

where $\Pi_{[0,1]}(t) := \min[1, \max[0, t]]$.

In sequential layer-wise quantization, \hat{W} is produced by a discrete rounding procedure. We therefore use (8) as a module-wise default: after quantizing a module, we compute $\alpha^*(\hat{W})$ from that module’s calibration features (X_f, X_q) and use it for the subsequent module. This yields an adaptive per-module schedule with negligible overhead.

3.2.2. STOCHASTIC SAMPLING RULE

To further regularize the calibration objective, we introduce *sequence-wise* flexibility in the interpolation parameter. Instead of using a single global α for the entire calibration set, we allow each calibration sequence $j \in \{1, \dots, N\}$ to have its own weight α_j , which controls how strongly the teacher activation is mixed into the student activation for that sequence. This stochastic formulation is not meant to approximate a sequence-wise optimal update, but to introduce randomness during calibration that regularizes the aggregated second-order statistics. We write $X_f = [X_f^{(1)}, \dots, X_f^{(N)}]$ and $X_q = [X_q^{(1)}, \dots, X_q^{(N)}]$, where $X_f^{(j)} \in \mathbb{R}^n$ and $X_q^{(j)} \in \mathbb{R}^n$ denote the j -th column (i.e., the activation vector corresponding to the j -th calibration sequence) of the teacher and student activation matrices, respectively.

While Section 3.2.1 admits a closed-form update for a single global α , using a sequence-wise counterpart (α_j) is impractical in a layer-wise pipeline: calibration relies on aggregated second-order activation moments, and a deterministic update would require retaining sequence-specific curvature information until \hat{W} is obtained. We therefore

adopt a stochastic rule that injects sequence-wise variation in α_j during second-order statistics accumulation, motivated by Mixup (Zhang et al., 2018). Specifically, for each calibration sequence j , we sample

$$\beta_j \sim \text{Beta}(\lambda, \lambda), \quad \alpha_j := \min[\beta_j, 1 - \beta_j] \in [0, 1/2], \quad (9)$$

where folding enforces $\alpha_j \leq 1/2$ and thus keeps the correction ratio $\alpha_j/(1 - \alpha_j) \leq 1$, matching the regime we target in practice. The α -weighted activation for sequence j is then given by

$$X_\alpha^{(j)} = (1 - \alpha_j)X_q^{(j)} + \alpha_j X_f^{(j)} = X_q^{(j)} + \alpha_j \Delta X^{(j)}, \quad (10)$$

and stacking columns yields $X_\alpha = [X_\alpha^{(1)}, \dots, X_\alpha^{(N)}]$. As shown in Fig. 3, sampling α yields lower run-to-run variability compared to using a fixed $\alpha = \mathbb{E}[\alpha]$; Section B.3 interprets this as adding a zero-mean dither to the shifted target before the discrete rounding map, which reduces calibration-induced variance.

4. Successive Rounding under Regularization

4.1. Rewriting the Asymmetric Objective

We begin with the regularized calibration objective

$$\mathcal{L}(\hat{W}; \alpha) = \|WX_\alpha - \hat{W}X_q\|_F^2. \quad (11)$$

To reveal its quadratic structure, define the Hessian $H := X_q X_q^\top \in \mathbb{R}^{n \times n}$ and the associated second-order matrices

$$\tilde{H}_\alpha := X_\alpha X_\alpha^\top, \quad C_\alpha := X_\alpha X_q^\top. \quad (12)$$

By construction, H is symmetric positive semidefinite; in practice, we apply standard damping (e.g., $H \leftarrow H + \lambda I$) to ensure $H \succ 0$, so that the linear solutions below are well-defined (Frantar et al., 2022).

A shifted least-squares proxy. The next theorem rewrites (11) as a Hessian-weighted least-squares problem with a *shifted target*.

Theorem 4.1 (Regularized calibration as least-squares problem). *Assume $H \in \mathbb{R}^{n \times n}$ is symmetric positive definite and let $H = LL^\top$ be its Cholesky decomposition. Define the shifted target matrix $M_\alpha = WC_\alpha H^{-1} \in \mathbb{R}^{m \times n}$. Then minimizing (11) over \hat{W} is equivalent to*

$$\min_{\hat{W}} \|(\hat{W} - M_\alpha)L\|_F^2. \quad (13)$$

Proof. Using $\|A\|_F^2 = \text{tr}(AA^\top)$ and cyclicity of the trace,

$$\begin{aligned} \mathcal{L}(\hat{W}; \alpha) &= \text{tr}[(WX_\alpha - \hat{W}X_q)(WX_\alpha - \hat{W}X_q)^\top] \\ &= \text{tr}(W\tilde{H}_\alpha W^\top) - 2\text{tr}(\hat{W}C_\alpha^\top W^\top) + \text{tr}(\hat{W}H\hat{W}^\top). \end{aligned}$$

The first term is constant in \hat{W} . Let $M_\alpha = WC_\alpha H^{-1}$. Since H is symmetric, $M_\alpha^\top = H^{-1}C_\alpha^\top W^\top$ and thus $HM_\alpha^\top = C_\alpha^\top W^\top$. Completing the square yields

$$\begin{aligned} \text{tr}(\hat{W}H\hat{W}^\top) - 2\text{tr}(\hat{W}C_\alpha^\top W^\top) \\ = \text{tr}[(\hat{W} - M_\alpha)H(\hat{W} - M_\alpha)^\top] + \text{const}, \end{aligned}$$

and substituting $H = LL^\top$ gives (13). \square

Theorem 4.1 shows that regularized calibration preserves the standard Hessian-weighted quadratic proxy, with rounding performed around the shifted target M_α instead of W .

4.2. Rounding via Triangular Discrete Least Squares

Following Theorem 4.1, rounding a layer amounts to solving

$$\min_{Q \in \mathcal{Q}} \|Q - M_\alpha\|_F^2, \quad (14)$$

where $Q \in \mathbb{R}^{m \times n}$ is a quantized weight matrix with entries constrained to the quantization grid \mathcal{Q} , $M_\alpha \in \mathbb{R}^{m \times n}$ is the shifted target matrix. The objective in (14) decomposes over rows as

$$\|Q - M_\alpha\|_F^2 = \sum_{i=1}^m \|(Q_{i,:} - M_{\alpha,i,:})L\|_2^2. \quad (15)$$

Let $R := L^\top \in \mathbb{R}^{n \times n}$ (upper triangular), $q_i := Q_{i,:}^\top \in \mathbb{R}^n$, and $y_i := R M_{\alpha,i,:}^\top \in \mathbb{R}^n$. Then the problem reduces to a row-wise triangular discrete least-squares problem

$$\min_{q_i \in \mathcal{Q}_i} \mathcal{L}(q_i) = \|Rq_i - y_i\|_2^2, \quad \forall i \in [m] \quad (16)$$

where \mathcal{Q}_i denotes the induced discrete set for row i . We now describe the rounding algorithms for a single row, dropping the subscript i for brevity. Expanding (16) yields

$$\|Rq - y\|_2^2 = \sum_{j=1}^n \left(y_j - \sum_{k=j}^n R_{j,k} q_k \right)^2. \quad (17)$$

Suppose the last $n - j$ coordinates $q_{j+1:n}$ are fixed. For $j \in \{1, \dots, n-1\}$, define the suffix-conditioned center

$$c_j(q_{j+1:n}) := \frac{y_j - \sum_{k=j+1}^n R_{j,k} q_k}{R_{j,j}}. \quad (18)$$

with $c_n := y_n/R_{n,n}$ (empty sum). Conditioned on $q_{j+1:n}$, choosing q_j incurs the incremental cost

$$\Delta_j(q_j \mid q_{j+1:n}) = R_{j,j}^2 |q_j - c_j(q_{j+1:n})|^2, \quad (19)$$

so the full row objective diagonalizes as

$$\mathcal{L}(q) = \|Rq - y\|_2^2 = \sum_{j=1}^n \Delta_j(q_j \mid q_{j+1:n}). \quad (20)$$

This formulation immediately leads to a greedy reverse-order rounding rule, as well as a bounded-search variant that retains multiple suffix candidates.

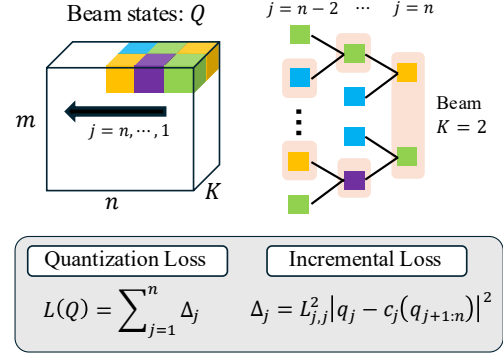


Figure 4. Overview of K -SNRQ beam search. Columns of the weight matrix are quantized sequentially from $j = n$ to 1, maintaining a beam of size K . At each step, candidate extensions are scored using the incremental loss and pruned to the top- K beams.

4.2.1. GREEDY ROUNDING: SNRQ

At level j , given the suffix $q_{j+1:n}$, the *greedy rounding* is the exact minimizer of the conditional discrete subproblem induced by (19),

$$q_j^*(q_{j+1:n}) \in \arg \min_{q \in \mathcal{Q}_j} |q - c_j(q_{j+1:n})|^2, \quad (21)$$

i.e., c_j is rounded to its nearest quantization level. Applying (21) successively for $j = n, n-1, \dots, 1$ produces a single sequence of quantization decisions; we refer to this as *Sequential Nearest-level Regularized Quantization (SNRQ)*.

Implementation. All rows share R , so we may quantize them in parallel. We present equivalent columnwise formulation in Theorem A.1, further be used in Algorithm 1.

4.2.2. K-BEST BEAM SEARCH: K-SNRQ

SNRQ commits to a single greedy sequence of quantization decisions in the triangular discrete least-squares problem (16). When the off-diagonal interactions encoded in R are non-negligible, early greedy choices can overly constrain subsequent decisions and lead to suboptimal solutions. We therefore introduce a bounded tree search procedure, K -SNRQ, which maintains the best K partial quantization sequences under the *exact* objective.

Rowwise K -best formulation. Because (14) decomposes over output rows (Eq. (15)), we apply K -SNRQ independently to each row problem (16), and batch the computation over rows. For a single row, recall the suffix-conditioned center $c_j(q_{j+1:n})$ in (18) and the branch metric $\Delta_j(q_j \mid q_{j+1:n})$ in (19). Decoding in reverse order, a beam state at level j is represented by a set of partial rounding decisions $q_{j+1:n}$ together with its accumulated score

$$S_{j+1}(q_{j+1:n}) := \sum_{t=j+1}^n \Delta_t(q_t \mid q_{t+1:n}). \quad (22)$$

Table 1. Per-group symmetric weight quantization (group size 128) for LLaMA 2/3 models. Reporting Wiki2/C4 perplexity (\downarrow), average zero-shot accuracy over six tasks (\uparrow), and end-to-end quantization time; SNRQ-C uses closed-form α , SNRQ-S uses stochastic sampling.

Model	Bits	Method	Wiki2 (\downarrow)	C4 (\downarrow)	WinoG	PIQA	HellaS	BoolQ	ArcE	ArcC	Avg.Acc (\uparrow)	Q.Time (s)
L3-8B	3	FP16	6.14	8.93	73.32	80.90	79.23	81.31	77.74	53.33	74.31	
		GPTQ	9.87	12.74	69.14	75.52	73.07	73.76	67.10	42.32	66.82	547.5
		GPTAQ	9.07	12.15	69.66	74.70	73.89	74.75	61.89	39.76	65.77	715.0
		LDLQ	14.99	14.12	69.82	74.97	70.81	71.27	63.47	40.84	65.20	472.5
		SNRQ-C	8.74	11.87	70.48	76.43	73.06	76.36	67.54	41.76	67.60	492.3
		SNRQ-S	8.55	11.73	70.64	77.56	73.28	77.55	71.62	45.36	69.33	484.7
	4	GPTQ	6.65	9.53	73.51	80.19	77.97	80.28	76.00	49.95	72.98	489.0
		GPTAQ	6.62	9.49	73.69	80.34	78.16	79.99	76.48	50.70	73.23	703.2
		LDLQ	6.66	9.52	73.16	80.12	78.14	79.58	76.67	50.61	73.05	425.1
		SNRQ-C	6.58	9.44	73.09	80.27	77.83	79.94	76.62	50.72	73.08	495.2
		SNRQ-S	6.58	9.44	73.24	80.23	77.88	80.18	76.76	51.26	73.26	498.7
L2-7B	3	FP16	5.47	6.97	69.06	79.11	75.98	77.74	74.62	46.33	70.47	
		GPTQ	6.75	8.26	65.97	76.71	71.88	73.11	67.93	41.21	66.14	467.9
		GPTAQ	6.57	8.04	66.71	77.27	72.00	73.10	68.11	40.84	66.34	590.4
		LDLQ	6.64	8.12	66.84	77.02	71.73	74.12	68.49	40.79	66.50	427.8
		SNRQ-C	6.41	7.89	67.48	77.68	71.55	72.94	70.02	41.26	66.82	407.4
		SNRQ-S	6.40	7.88	68.02	77.40	71.69	75.07	70.18	41.37	67.34	417.3
	4	GPTQ	5.68	7.16	69.14	78.40	75.11	77.25	73.13	44.47	69.58	481.6
		GPTAQ	5.66	7.14	69.72	78.52	75.16	75.32	73.30	44.57	69.43	610.5
		LDLQ	5.67	7.16	69.69	78.44	75.21	76.77	73.04	44.11	69.54	404.8
		SNRQ-C	5.64	7.12	68.83	78.56	75.07	76.20	73.49	44.81	69.49	450.9
		SNRQ-S	5.64	7.12	69.20	78.58	75.14	76.41	73.47	45.07	69.65	405.6
L2-13B	3	FP16	4.88	6.47	72.30	80.52	79.38	80.58	77.53	49.06	73.23	
		GPTQ	5.60	7.16	70.54	79.27	76.32	79.08	73.91	46.45	70.93	820.5
		GPTAQ	5.54	7.10	70.83	79.36	76.36	79.05	74.11	46.42	71.00	1012.0
		LDLQ	5.57	7.12	70.26	79.11	76.24	78.94	74.80	46.47	70.97	719.2
		SNRQ-C	5.57	7.10	70.69	79.44	76.03	78.33	75.18	46.72	71.06	749.6
		SNRQ-S	5.52	7.07	71.19	79.07	75.95	78.85	74.94	46.63	71.11	724.2
	4	GPTQ	5.02	6.59	72.06	79.91	78.78	79.42	76.83	48.72	72.62	727.7
		GPTAQ	5.01	6.57	71.87	79.83	78.80	80.09	76.88	48.82	72.71	1019.2
		LDLQ	5.01	6.58	72.58	79.87	78.75	79.98	76.79	48.75	72.79	623.9
		SNRQ-C	5.00	6.57	72.38	80.11	78.65	79.86	76.95	48.82	72.80	726.1
		SNRQ-S	5.01	6.57	72.06	79.99	78.75	79.79	76.69	48.75	72.67	709.4

To advance one level, we enumerate candidates q_j for each beam state, score each expansion by $S_{j+1}(q_{j+1:n}) + \Delta_j(q_j \mid q_{j+1:n})$, and retain the best K expansions (see Fig. 4). Setting $K = 1$ recovers SNRQ. Each q_j ranges over the grid \mathcal{Q}_j (e.g., 2^b uniformly spaced codes for b -bit quantization).

Batched implementation. Since the objective decomposes across rows (see (16)), beam search can be performed independently for all rows, analogously to SNRQ. We therefore maintain tensorized beam states and perform level-wise expansion, followed by a single `topk` pruning operation per level. See Algorithm 3 and Section A.2 for details.

5. Results

We present the main results on regularized sequential rounding (SNRQ) in Section 5.2, and the additional gains from bounded beam-search (K-SNRQ) in Section 5.3, highlighting the trade-off between quantization quality and complexity. Additional ablations on (i) the sampling parameter in SNRQ-S and (ii) the interaction between calibration and rounding are provided in Section C.1.

5.1. Setup

We evaluate **SNRQ** for post-training quantization (PTQ) of decoder-only LLMs, including LLaMA 2/3 (Touvron et al., 2023; Grattafiori et al., 2024), Qwen3-8B (Yang et al., 2025), and Phi-3 Mini (3.8B) (Abdin et al., 2024). We use 128 samples from the C4 dataset with a sequence length of

2048 for calibration. We report (i) perplexity (PPL) on WikiText2 and C4, and (ii) zero-shot accuracy on six standard commonsense reasoning tasks: WinoGrande (Sakaguchi et al., 2021), PIQA (Bisk et al., 2020), HellaSwag (Zellers et al., 2019), BoolQ (Clark et al., 2019), ARC-Easy, and ARC-Challenge (Clark et al., 2018). Results are averaged over 5 seeds, and quantization time is reported as end-to-end wall-clock runtime measured on a single H200 GPU, which includes non-GPU overhead.

We compare against learning-free PTQ baselines: GPTQ (Frantar et al., 2022), GPTAQ (Li et al., 2025) (with $\alpha = 0.25$, as used in the official implementation), and LDLQ (Chee et al., 2023). For per-channel quantization, we additionally include GuidedQuant (Kim et al., 2025) for comparison, which does not support per-group quantization in the official implementation. We report two versions of our method: SNRQ-C (closed-form α) and SNRQ-S (sampling), using $\lambda = 5.0$ by default for SNRQ-S.

5.2. Performance Evaluation

Per-group quantization. Table 1 summarizes per-group weight-only quantization with groupsize 128 for Llama 2/3 models (Touvron et al., 2023; Grattafiori et al., 2024). Across all models, SNRQ variants consistently improve perplexity and downstream accuracy compared to baselines. For example, on 3-bit LLaMA3-8B, SNRQ-S reduces perplexity by 5.7% on Wiki2 and 3.5% on C4 relative to GPTAQ, while improving zero-shot accuracy by 5.4%. Cru-

Table 2. 3-bit per-channel weight-only quantization. Reporting perplexity, average zero-shot accuracy, and quantization time.

Model	Method	Wiki2 (↓)	C4 (↓)	Avg.Acc (↑)	Q.Time (s)
L3-8B	GPTQ	24.80	23.59	51.68	550.1
	GPTAQ	33.47	22.00	51.61	701.4
	LDLQ	24.65	23.16	51.02	457.4
	GuidedQ	49.79	40.03	48.58	2110.1
	SNRQ-C	17.78	19.10	55.16	486.2
	SNRQ-S	18.03	19.98	56.33	480.6
L2-7B	GPTQ	9.36	10.71	59.41	461.5
	GPTAQ	8.72	10.01	60.91	578.4
	LDLQ	9.42	10.65	60.08	401.8
	GuidedQ	9.01	10.26	61.83	1883.0
	SNRQ-C	8.65	9.62	62.16	406.6
	SNRQ-S	9.05	9.62	62.10	394.8
L2-13B	GPTQ	6.90	8.36	66.26	763.7
	GPTAQ	6.70	8.20	66.83	1015.8
	LDLQ	6.87	8.32	66.97	704.2
	GuidedQ	6.94	8.37	67.18	3170.4
	SNRQ-C	6.51	7.99	67.77	717.4
	SNRQ-S	6.58	8.01	67.56	700.1

Table 3. Weight-activation-KV cache quantization with SpinQuant. Reporting Wiki2 perplexity and quantization time for W4A4KV4 and W4A4KV16. For GuidedQ, time excludes Hessian estimation.

Bits	Methods	L3-8B		L2-7B		L2-13B	
		Wiki2	T (s)	Wiki2	T (s)	Wiki2	T (s)
W4A4KV4	SpinQuant	7.37	577	5.95	521	5.24	878
	+GPTAQ	7.30	844	5.90	753	5.22	1121
	+GuidedQ*	7.31	585	5.89	515	5.19	842
	+SNRQ-S	7.26	592	5.88	508	5.18	872
W4A4KV16	SpinQuant	7.28	573	5.89	523	5.21	829
	+GPTAQ	7.20	800	5.85	710	5.19	1123
	+GuidedQ*	7.21	595	5.85	529	5.17	856
	+SNRQ-S	7.19	610	5.82	497	5.16	868

cially, these improvements are achieved with substantially lower quantization time than GPTAQ across all model sizes, yielding a **29–32% speedup** while simultaneously improving performance. This efficiency stems from the structure of the proposed rounding procedure, which avoids repeated factorizations during calibration. While SNRQ-S consistently outperforms SNRQ-C, both variants exhibit a desirable accuracy–runtime trade-off, incurring only negligible additional overhead, as quantified in Table 12.

Per-channel quantization. Per-channel weight quantization is more challenging than per-group quantization since all entries in a row share the same scale and zero-point, which amplifies the impact of local rounding errors. Table 2 shows that SNRQ substantially improves robustness to rounding errors in this regime. Relative to GPTQ, SNRQ reduces Wiki2 perplexity by up to 28% on L3-8B, 8% on L2-7B, and 6% on L2-13B. Compared to GPTAQ, the gains are most pronounced on L3-8B, where SNRQ achieves about 46% lower Wiki2 perplexity and 13% lower C4 perplexity. SNRQ keeps quantization time comparable to GPTQ/LDLQ and substantially lower than GuidedQuant.

Results with outlier reductions. We evaluate SNRQ as a replacement for the weight-only refinement stage in weight-

Table 4. 3-bit weight-only quantization results of Qwen3-8B and Phi3-3.8B models. Best results and those within one standard deviation of the best are highlighted.

Model	Method	Wiki2 (↓)	C4 (↓)	Avg.Acc (↑)	Q.Time (s)
Qwen3-8B	FP16	9.73	14.65	74.15	–
	GPTQ	11.75	15.09	68.49	494.9
	GPTAQ	11.95	15.13	68.94	670.4
	LDLQ	11.41	14.65	69.26	419.5
	SNRQ-C	11.65	14.98	70.05	480.2
	SNRQ-S	11.34	14.66	70.56	478.4
Phi3-3.8B	FP16	6.01	9.11	75.41	–
	GPTQ	8.84	11.31	67.84	262.7
	GPTAQ	8.45	10.97	68.74	332.0
	LDLQ	9.07	11.46	67.01	231.9
	SNRQ-C	8.35	10.78	68.47	271.4
	SNRQ-S	8.23	10.74	69.00	267.7

activation–KV cache quantization pipelines using SpinQuant (Liu et al., 2024), which mitigates outliers using learned rotation matrices. We use 128 samples from WikiText2 for calibration and perform per-channel symmetric quantization for weights, and per-group asymmetric quantization for activations and KV caches. As shown in Table 3, SpinQuant+SNRQ-S consistently improves upon SpinQuant across both W4A4KV4 and W4A4KV16 settings, without incurring the substantial runtime overhead. This indicates that the benefits of SNRQ extend beyond weight-only quantization and carry over to integrated pipelines where activation and KV quantization further constrain accuracy.

Different model architectures. Beyond LLaMa, Table 4 shows that SNRQ transfers well to other architectures. On Qwen3-8B, SNRQ-S reduces Wiki2 perplexity by approximately 5.1% relative to GPTAQ, while improving zero-shot accuracy by roughly 2.3%; it also matches the best C4 perplexity within a negligible margin. On Phi3-3.8B, SNRQ-S reduces Wiki2 and C4 perplexities by about 2% relative to GPTAQ and improves accuracy by about 0.4%, while maintaining quantization time comparable to GPTQ and approximately 20% faster than GPTAQ. These results indicate that SNRQ improves both perplexity and accuracy across diverse model families without incurring additional quantization cost relative to the baselines.

5.3. Quantization performance-cost trade-off

We next evaluate the beam search extension, K -SNRQ, which trades additional search computation for improved rounding quality under the triangular proxy. Figures 5 and 9 (Appendix) illustrate this trade-off for 3-bit quantization by plotting perplexity against quantization time and peak GPU memory for L2-7B and L2-13B across beam widths. Increasing K yields consistent perplexity reductions and forms a clear Pareto frontier: larger beams incur higher compute and peak memory but achieve better rounding quality than the greedy path ($K = 1$). With our batched implementation, search time varies only slightly with K , while peak GPU

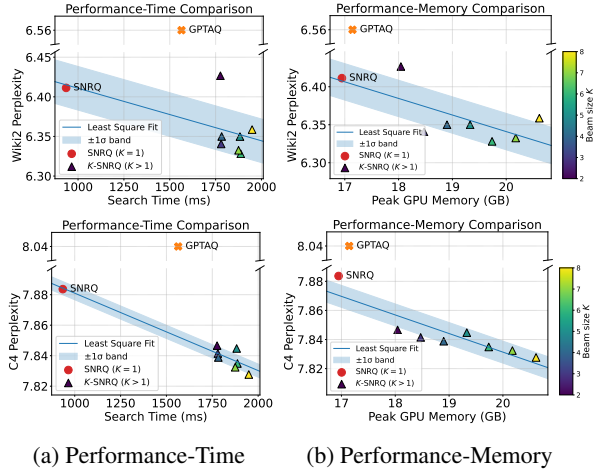


Figure 5. Performance-efficiency trade-offs of K -SNRQ for 3-bit L2-7B. Wiki2 and C4 perplexity versus quantization time (left) and peak GPU memory (right) as beam width K increases.

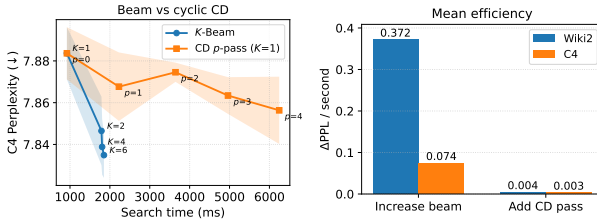


Figure 6. (Left) C4 perplexity vs. search time for increasing beam width K and additional CD passes, with ± 1 standard deviation shaded. (Right) Mean marginal perplexity improvement per second for beam expansion versus additional CD passes.

memory grows due to the expanded beam state. Overall, beam search closes a substantial fraction of the remaining quality gap, suggesting that residual error is often caused by decisions that benefit from limited lookahead. We further provide an ablation that isolates the effect of discrete search under different calibration in Section C.1.2.

Comparison of rounding algorithms. To evaluate the effectiveness of K -SNRQ, we compare it against cyclic coordinate-descent (CD) refinement applied as a post-processing step after SNRQ/ K -SNRQ (Chee et al., 2023; Behdin et al., 2023). Figure 6 (left) plots perplexity versus search time when increasing either the beam width K or the number of CD passes p . Increasing K yields larger perplexity reductions for a modest increase in runtime, whereas additional CD passes incur substantially higher overhead for smaller gains. Figure 6 (right) summarizes this trend using the mean marginal improvement per second (full results in Table 13), computed as $\Delta \text{PPL}/\Delta t$ for each incremental update and averaged across steps. Overall, these results indicate that beam search provides a more favorable accuracy–runtime trade-off than CD refinement.

6. Related Work

6.1. Layer-wise Optimization for PTQ

Given calibration data, a widely used family of post-training quantization minimizes a quadratic reconstruction error that measures the layer’s output distortion under a second-order (Hessian) surrogate (Nagel et al., 2020; Hubara et al., 2021; Li et al., 2021), with GPTQ being a widely adopted LLM-scale realization (Frantar et al., 2022). Beyond purely local reconstruction, several recent works aim to incorporate information about the end-to-end model behavior. OAC introduces an output-adaptive calibration objective motivated by output cross-entropy distortion and derives tractable approximations for layerwise optimization (Edalati et al., 2025). GuidedQuant integrates end-loss gradient information into the objective while modeling cross-weight dependencies within output channels, improving multiple PTQ settings (Kim et al., 2025). YAQA further targets end-to-end distribution preservation by using Kronecker-factored approximations of a layer’s Hessian with respect to the full-model KL divergence and provides adaptive rounding guarantees (Tseng et al., 2025). A complementary and orthogonal line of work focuses on *error propagation* in sequential PTQ. GPTAQ resolves this mismatch with asymmetric calibration and derives efficient block-wise closed-form updates on top of GPTQ (Li et al., 2025). ApiQ adopts a related asymmetric objective, but leverages it in a learning-based pipeline that jointly optimizes quantized weights and LoRA adapters before downstream finetuning (Liao et al., 2024).

6.2. Rounding and Discrete Solvers for PTQ

Given a Hessian-based quadratic reconstruction objective, PTQ for LLMs reduces to a discrete optimization problem over low-bit weights. GPTQ applies sequential greedy rounding with error-feedback using a Hessian factorization (Frantar et al., 2022), while QuIP derives an equivalent but more efficient solver (LDLQ) (Chee et al., 2023). Beyond greedy rounding, QuantEase and CDQuant improve solutions via coordinate-descent refinement, trading additional objective evaluations for better reconstruction (Behdin et al., 2023; Nair & Suggala, 2024). Recent geometric analyses interpret GPTQ as an instance of Babai’s nearest-plane method for the closest vector problem (Chen et al., 2025).

Beyond scalar, column-wise rounding, vector quantization (VQ) jointly quantizes weight blocks using learned codebooks, shifting the discrete problem from per-weight rounding to structured code decoding and typically incurring higher inference complexity. AQLM adapts additive quantization to LLMs via alternating updates of codebooks and assignments (Egiazarian et al., 2024), and uses beam search to select combinations of codewords during decoding. In contrast, our beam search operates over successive *column-wise rounding decisions* induced by least-squares proxy

with triangular coupling, rather than over codebook assignments. Other recent VQ solvers include QuIP# and GPTVQ, which extend column-wise updates to block-wise quantization (Tseng et al., 2024; Van Baalen et al., 2024).

7. Conclusion

We presented a post-training quantization framework that connects objective design with the structure of the discrete rounding problem. By introducing a regularized proxy that decomposes into symmetric reconstruction and asymmetric regularization, we enable controlled asymmetry while preserving the quadratic form required for efficient solvers. Building on this formulation, we derive a sequential rounding algorithm for minimizing a triangular least-squares proxy, with a bounded-search extension that enables an explicit quality–computation trade-off. Experiments indicate that regularized calibration, when paired with solvers that exploit the induced discrete structure, provides a practical and scalable path to improved LLM quantization.

References

Abdin, M. et al. Phi-3 technical report: A highly capable language model locally on your phone, 2024. URL <https://arxiv.org/abs/2404.14219>.

Behdin, K., Acharya, A., Gupta, A., Selvaraj, S. K., and Mazumder, R. Quantease: Optimization-based quantization for language models—an efficient and intuitive algorithm. *CoRR*, 2023.

Bisk, Y., Zellers, R., Gao, J., Choi, Y., et al. Piqa: Reasoning about physical commonsense in natural language. In *Proceedings of the AAAI conference on artificial intelligence*, volume 34, pp. 7432–7439, 2020.

Chee, J., Cai, Y., Kuleshov, V., and De Sa, C. M. Quip: 2-bit quantization of large language models with guarantees. *Advances in Neural Information Processing Systems*, 36: 4396–4429, 2023.

Chen, J., Shabanzadeh, Y., Crnčević, E., Hoefer, T., and Alistarh, D. The geometry of llm quantization: Gptq as babai’s nearest plane algorithm. *arXiv preprint arXiv:2507.18553*, 2025.

Clark, C., Lee, K., Chang, M.-W., Kwiatkowski, T., Collins, M., and Toutanova, K. Boolq: Exploring the surprising difficulty of natural yes/no questions. *arXiv preprint arXiv:1905.10044*, 2019.

Clark, P., Cowhey, I., Etzioni, O., Khot, T., Sabharwal, A., Schoenick, C., and Tafjord, O. Think you have solved question answering? try arc, the ai2 reasoning challenge. *arXiv preprint arXiv:1803.05457*, 2018.

Ding, X., Liu, X., Tu, Z., Zhang, Y., Li, W., Hu, J., Chen, H., Tang, Y., Xiong, Z., Yin, B., et al. Cbq: Cross-block quantization for large language models. *arXiv preprint arXiv:2312.07950*, 2023.

Edalati, A., Ghaffari, A., Nejad, M. G., Hou, L., Chen, B., Asgharian, M., and Nia, V. P. Oac: Output-adaptive calibration for accurate post-training quantization. In *Proceedings of the AAAI Conference on Artificial Intelligence*, volume 39, pp. 16453–16461, 2025.

Egiazarian, V., Panferov, A., Kuznedelev, D., Frantar, E., Babenko, A., and Alistarh, D. Extreme compression of large language models via additive quantization. *arXiv preprint arXiv:2401.06118*, 2024.

Frantar, E. and Alistarh, D. Optimal brain compression: A framework for accurate post-training quantization and pruning. *Advances in Neural Information Processing Systems*, 35:4475–4488, 2022.

Frantar, E., Ashkboos, S., Hoefer, T., and Alistarh, D. Gptq: Accurate post-training quantization for generative pre-trained transformers. *arXiv preprint arXiv:2210.17323*, 2022.

Ge, Y., Hua, W., Mei, K., Tan, J., Xu, S., Li, Z., Zhang, Y., et al. Openagi: When llm meets domain experts. *Advances in Neural Information Processing Systems*, 36: 5539–5568, 2023.

Gholami, A., Yao, Z., Kim, S., Hooper, C., Mahoney, M. W., and Keutzer, K. Ai and memory wall. *IEEE Micro*, 44(3):33–39, 2024.

Grattafiori, A., Dubey, A., Jauhri, A., Pandey, A., Kadian, A., Al-Dahle, A., Letman, A., Mathur, A., Schelten, A., Vaughan, A., et al. The llama 3 herd of models. *arXiv preprint arXiv:2407.21783*, 2024.

Hubara, I., Nahshan, Y., Hanani, Y., Banner, R., and Soudry, D. Accurate post training quantization with small calibration sets. In *International conference on machine learning*, pp. 4466–4475. PMLR, 2021.

Kim, J., Kim, H.-y., Cho, E., Lee, C., Kim, J., and Jeon, Y. Boa: Attention-aware post-training quantization without backpropagation. *arXiv preprint arXiv:2406.13474*, 2024.

Kim, J., El Halabi, M., Park, W., Schaefer, C. J., Lee, D., Park, Y., Lee, J. W., and Song, H. O. Guidedquant: Large language model quantization via exploiting end loss guidance. In *Forty-second International Conference on Machine Learning*, 2025.

Kim, S., Hooper, C., Gholami, A., Dong, Z., Li, X., Shen, S., Mahoney, M. W., and Keutzer, K. Squeezellm: Dense-and-sparse quantization. *arXiv preprint arXiv:2306.07629*, 2023.

Li, Y., Gong, R., Tan, X., Yang, Y., Hu, P., Zhang, Q., Yu, F., Wang, W., and Gu, S. Brecq: Pushing the limit of post-training quantization by block reconstruction. *arXiv preprint arXiv:2102.05426*, 2021.

Li, Y., Yin, R., Lee, D., Xiao, S., and Panda, P. Gptaq: Efficient finetuning-free quantization for asymmetric calibration. In *Forty-second International Conference on Machine Learning*, 2025.

Liao, B., Herold, C., Khadivi, S., and Monz, C. Apiq: Finetuning of 2-bit quantized large language model. *arXiv preprint arXiv:2402.05147*, 2024.

Liu, Z., Zhao, C., Fedorov, I., Soran, B., Choudhary, D., Krishnamoorthi, R., Chandra, V., Tian, Y., and Blankevoort, T. Spinquant: Llm quantization with learned rotations. *arXiv preprint arXiv:2405.16406*, 2024.

Nagel, M., Amjad, R. A., Van Baalen, M., Louizos, C., and Blankevoort, T. Up or down? adaptive rounding for post-training quantization. In *International conference on machine learning*, pp. 7197–7206. PMLR, 2020.

Nair, P. A. and Suggala, A. S. Cdquant: Greedy coordinate descent for accurate llm quantization. *arXiv preprint arXiv:2406.17542*, 2024.

Nam, D., Macvean, A., Hellendoorn, V., Vasilescu, B., and Myers, B. Using an llm to help with code understanding. In *Proceedings of the IEEE/ACM 46th International Conference on Software Engineering*, pp. 1–13, 2024.

Sakaguchi, K., Bras, R. L., Bhagavatula, C., and Choi, Y. Winogrande: An adversarial winograd schema challenge at scale. *Communications of the ACM*, 64(9):99–106, 2021.

Touvron, H., Cord, M., Douze, M., Massa, F., Sablayrolles, A., and Jégou, H. Training data-efficient image transformers & distillation through attention. In *International conference on machine learning*, pp. 10347–10357. PMLR, 2021.

Touvron, H., Lavril, T., Izacard, G., Martinet, X., Lachaux, M.-A., Lacroix, T., Rozière, B., Goyal, N., Hambro, E., Azhar, F., et al. Llama: Open and efficient foundation language models. *arXiv preprint arXiv:2302.13971*, 2023.

Tseng, A., Chee, J., Sun, Q., Kuleshov, V., and De Sa, C. Quip #: Even better llm quantization with hadamard incoherence and lattice codebooks. In *International Conference on Machine Learning*, pp. 48630–48656. PMLR, 2024.

Tseng, A., Sun, Z., and De Sa, C. Model-preserving adaptive rounding. *arXiv preprint arXiv:2505.22988*, 2025.

Van Baalen, M., Kuzmin, A., Koryakovskiy, I., Nagel, M., Couperus, P., Bastoul, C., Mahurin, E., Blankevoort, T., and Whatmough, P. Gptvq: The blessing of dimensionality for llm quantization. *arXiv preprint arXiv:2402.15319*, 2024.

Xu, J., Li, Z., Chen, W., Wang, Q., Gao, X., Cai, Q., and Ling, Z. On-device language models: A comprehensive review. *arXiv preprint arXiv:2409.00088*, 2024.

Yang, A., Li, A., Yang, B., Zhang, B., Hui, B., Zheng, B., Yu, B., Gao, C., Huang, C., Lv, C., et al. Qwen3 technical report. *arXiv preprint arXiv:2505.09388*, 2025.

Yang, J., Jin, H., Tang, R., Han, X., Feng, Q., Jiang, H., Zhong, S., Yin, B., and Hu, X. Harnessing the power of llms in practice: A survey on chatgpt and beyond. *ACM Transactions on Knowledge Discovery from Data*, 18(6): 1–32, 2024.

Zellers, R., Holtzman, A., Bisk, Y., Farhadi, A., and Choi, Y. Hellaswag: Can a machine really finish your sentence? *arXiv preprint arXiv:1905.07830*, 2019.

Zhang, H., Cisse, M., Dauphin, Y. N., and Lopez-Paz, D. mixup: Beyond empirical risk minimization. In *International Conference on Learning Representations*, 2018.

Zheng, X., Qin, H., Li, Y., Chu, H., Wang, J., Guo, J., Magno, M., and Liu, X. First-order error matters: Accurate compensation for quantized large language models. *arXiv preprint arXiv:2507.11017*, 2025.

A. Algorithms

We provide pseudocode for SNRQ and K -SNRQ, together with practical implementation details that bridge the objective reformulation and search procedures used in our codebase. Specifically, Algorithm 1 presents the base SNRQ algorithm, while Algorithm 2 introduces its lazy-batch variant (Frantar et al., 2022). Building on the same triangular proxy, Algorithm 3 extends SNRQ to a K -best (beam) search that maintains multiple candidates per output row and enables a bounded-complexity improvement over greedy rounding.

To make the connection explicit, we first provide a matrix-level interpretation that shows how the Cholesky-triangular form yields a columnwise branch-metric decomposition with an interference-cancelled target (Theorem A.1), which directly motivates successive rounding and its beam-search generalization. We then detail our beam-search implementation.

A.1. Matrix-level interpretation of objective reformulation and successive rounding

Proposition A.1 (Columnwise decomposition of the triangular proxy). *Let $H \in \mathbb{R}^{n \times n}$ be SPD and admit a Cholesky factorization $H = LL^\top$ with L lower triangular and $L_{j,j} > 0$. Define $E := Q - M \in \mathbb{R}^{m \times n}$. Given calibration objective $\mathcal{L}(Q) = \|(Q - M)L\|_F^2$, we have*

$$\mathcal{L}(Q) = \|EL\|_F^2 = \sum_{j=1}^n L_{j,j}^2 \|E_{:,j} + \sum_{k=j+1}^n E_{:,k} \frac{L_{k,j}}{L_{j,j}}\|_2^2. \quad (23)$$

Equivalently, defining

$$\tilde{W}_{:,j} := M_{:,j} + \sum_{k=j+1}^n (M_{:,k} - Q_{:,k}) \frac{L_{k,j}}{L_{j,j}}, \quad (24)$$

we have the diagonalized form

$$\mathcal{L}(Q) = \sum_{j=1}^n L_{j,j}^2 \|\tilde{W}_{:,j} - Q_{:,j}\|_2^2. \quad (25)$$

Eq. (25) is precisely the branch-metric decomposition that appears in sphere decoding: $L_{j,j}^2$ acts as a per-level weight, and $\tilde{W}_{:,j}$ is the interference-cancelled (i.e., successive-cancellation) target for column j given already-chosen later columns $\{Q_{:,k}\}_{k>j}$. Thus, choosing Q corresponds to *traversing a tree* over columns $j = n, n-1, \dots, 1$ in which each decision fixes a column and updates the targets for earlier columns.

Proof. Let e_j denote the j -th standard basis vector in \mathbb{R}^n . The j -th column of EL is

$$(EL)_{:,j} = E L_{:,j} = \sum_{k=1}^n E_{:,k} L_{k,j}.$$

Since L is lower triangular, $L_{k,j} = 0$ for $k < j$, hence

$$(EL)_{:,j} = \sum_{k=j}^n E_{:,k} L_{k,j} = L_{j,j} \left(E_{:,j} + \sum_{k=j+1}^n E_{:,k} \frac{L_{k,j}}{L_{j,j}} \right).$$

Taking squared ℓ_2 norms and summing over j yields

$$\|EL\|_F^2 = \sum_{j=1}^n \|(EL)_{:,j}\|_2^2 = \sum_{j=1}^n L_{j,j}^2 \left\| E_{:,j} + \sum_{k=j+1}^n E_{:,k} \frac{L_{k,j}}{L_{j,j}} \right\|_2^2, \quad (26)$$

which proves (23). Substituting $E = Q - M$ and rearranging gives $\tilde{W}_{:,j} - Q_{:,j} = -(E_{:,j} + \sum_{k>j} E_{:,k} L_{k,j} / L_{j,j})$, and thus (25). \square

Algorithm 1 Sequential Nearest-Level Regularized Quantization (SNRQ)

Input: FP weight $\mathbf{W} \in \mathbb{R}^{m \times n}$, α -weighted input \mathbf{X}_α , student input \mathbf{X}_q , permutation matrix \mathbf{P}

Output: \mathbf{Q}

- 1 $\mathbf{H} \leftarrow (\mathbf{X}_q \mathbf{X}_q^\top + \lambda \mathbf{I})$, $\mathbf{C}_\alpha = \mathbf{X}_\alpha \mathbf{X}_q^\top$
- 2 $\mathbf{H} \leftarrow \mathbf{P}^\top \mathbf{H} \mathbf{P}$, $\mathbf{C}_\alpha \leftarrow \mathbf{P}^\top \mathbf{C}_\alpha \mathbf{P}$
- 3 $\mathbf{L} \leftarrow \text{CHOLESKY}(\mathbf{H})$
- 4 $\mathbf{L} \leftarrow \mathbf{L}/\text{diag}(\mathbf{L}) - \mathbf{I}$
- 5 $\mathbf{W} \leftarrow \mathbf{W} \mathbf{P}$
- 6 $\mathbf{M}_\alpha \leftarrow \mathbf{W} \mathbf{C}_\alpha \mathbf{H}^{-1}$, $\mathbf{Q} \leftarrow \mathbf{0}$, $\tilde{\mathbf{W}} \leftarrow \mathbf{0}$
- 7 **for** $j \leftarrow n-1$ to 0 **do**
- 8 $\tilde{\mathbf{W}}[:, j] \leftarrow \mathbf{M}_\alpha[:, j] + (\mathbf{M}_\alpha[:, j+1:] - \mathbf{Q}[:, j+1:]) \mathbf{L}[j+1 :, j]$
- 9 $\mathbf{Q}[:, j] \leftarrow \text{ROUND}(\tilde{\mathbf{W}}[:, j])$
- 10 **end**
- 11 $\mathbf{Q} \leftarrow \mathbf{Q} \mathbf{P}^\top$

Table 5. Dimensions of major tensors used in SNRQ and K -SNRQ rounding for one linear layer of shape $m \times n$. B is blocksize, K is beam width, and $A = 2^b$ is the number of quantization levels for b -bit rounding. Center correction T defined in Algorithm 2 is required for lazy-batch update.

Tensor	SNRQ ($K=1$)	K -SNRQ (beam)
Shifted target \mathbf{M}_α	$m \times n$	$m \times n$
Lower-triangular matrix \mathbf{L}	$n \times n$	$n \times n$
Quantized weight \mathbf{Q}	$m \times n$	selected at end
Beam scores \mathbf{S}	—	$m \times K$
Beam states \mathbf{Q}_{tail}	—	$m \times K \times n$
Per-step expansion cost Δ	—	$m \times K \times A$
Block target $\tilde{\mathbf{M}}_{\alpha, \text{blk}}$	$m \times B$	$m \times B$
Block lower-triangular matrix \mathbf{L}_{blk}	$m \times B$	$m \times B$
Block states \mathbf{Q}_{blk}	$m \times B$	$m \times K \times B$
Center correction T	$m \times B$	$m \times K \times B$

Permutation matrix \mathbf{P} The reformulation in Theorem B.1 also motivates a principled *column permutation* of the weight matrix prior to successive rounding. In (25), the proxy decomposes into level-wise contributions $L_{j,j}^2 \|\tilde{\mathbf{W}}[:,j] - \mathbf{Q}[:,j]\|_2^2$, where the weight $L_{j,j}^2$ reflects the local scaling induced by H . Since $\tilde{\mathbf{W}}[:,j]$ is an interference-cancelled target that depends on the already-fixed columns $\{\mathbf{Q}_{:,k}\}_{k>j}$, the overall procedure is inherently order-dependent: decisions made first establish the tail $\{\mathbf{Q}_{:,k}\}_{k>j}$ that conditions all subsequent targets. Consequently, it is advantageous to quantize the most influential columns early so that their values are fixed and consistently accounted for in the successive-cancellation updates of the remaining columns.

Accordingly, we define a permutation $\pi : [n] \rightarrow [n]$ that sorts coordinates as $H_{\pi(1),\pi(1)} \leq H_{\pi(2),\pi(2)} \leq \dots \leq H_{\pi(n),\pi(n)}$. We then apply this permutation to reorder the columns before running successive rounding with a right-to-left traversal $j = n, n-1, \dots, 1$. Under this convention, the coordinates with larger diagonal curvature H_{ii} are placed closer to the beginning of the decoding order and are therefore quantized first. This permutation is used throughout all of our implementations.

We note that this interpretation is exact only in the diagonal case: if H is diagonal, then its Cholesky factor satisfies $L = \text{diag}(\sqrt{H_{11}}, \dots, \sqrt{H_{nn}})$, so sorting by H_{ii} is equivalent to sorting by the true per-level weights $L_{j,j}^2$ in (25). When H is not diagonal, the diagonal entries H_{ii} no longer uniquely determine $L_{j,j}$ due to off-diagonal couplings. Nevertheless, in practice we find that ordering columns by the diagonal proxy H_{ii} yields a consistent and effective decoding order, serving as a simple curvature-based heuristic that remains well aligned with the dominant directions even in the presence of correlations.

Algorithm 2 Sequential Nearest-Level Regularized Quantization (SNRQ) with Lazy-Batch Update

Input: FP weight $\mathbf{W} \in \mathbb{R}^{m \times n}$, α -weighted input \mathbf{X}_α , student input \mathbf{X}_q , permutation matrix \mathbf{P} , Block size B

Output: \mathbf{Q}

```

22  $\mathbf{H} \leftarrow (\mathbf{X}_q \mathbf{X}_q^\top + \lambda \mathbf{I})$ ,  $\mathbf{C}_\alpha = \mathbf{X}_\alpha \mathbf{X}_\alpha^\top$ 
23  $\mathbf{H} \leftarrow \mathbf{P}^\top \mathbf{H} \mathbf{P}$ ,  $\mathbf{C}_\alpha \leftarrow \mathbf{P}^\top \mathbf{C}_\alpha \mathbf{P}$ 
24  $\mathbf{L} \leftarrow \text{CHOLESKY}(\mathbf{H})$ 
25  $\mathbf{L} \leftarrow \mathbf{L}/\text{diag}(\mathbf{L}) - \mathbf{I}$ 
26  $\mathbf{W} \leftarrow \mathbf{W} \mathbf{P}$ 
27  $\mathbf{M}_\alpha \leftarrow \mathbf{W} \mathbf{C}_\alpha \mathbf{H}^{-1}$ ,  $\mathbf{Q} \in \mathbb{R}^{m \times n} \leftarrow \mathbf{0}$ 
28 for  $i = n, n - B, n - 2B, \dots$  do
29    $\mathbf{T} = (\mathbf{M}_\alpha[:, i :] - \mathbf{Q}[:, i :]) \mathbf{L}[i, i - B : i]$ 
30    $\tilde{\mathbf{W}} \in \mathbb{R}^{m \times B} \leftarrow \mathbf{0}$ 
31   for  $j = B - 1, B - 2, \dots, 0$  do
32      $\tilde{\mathbf{W}}[:, j] \leftarrow \mathbf{M}_\alpha[:, i - B + j]$ 
33      $+ (\mathbf{M}_\alpha[:, i - B : i] - \mathbf{Q}[:, i - B : i]) \mathbf{L}[i - B : i, i - B + j]$ 
34      $+ \mathbf{T}[:, j]$ 
35      $\mathbf{Q}[:, i - B + j] \leftarrow \text{ROUND}(\tilde{\mathbf{W}}[:, j])$ 
36   end
37 end
38  $\mathbf{Q} \leftarrow \mathbf{Q} \mathbf{P}^\top$ 

```

A.2. Beam Search Implementation

At a given level (column) $j = n, \dots, 1$, for each row and beam, we form the interference-cancelled target (the “center”) using the triangular couplings. In the columnwise batched form, this corresponds to the $\tilde{\mathbf{W}}_{:,j}$ update in (24). In our code, we compute the same quantity as a *beam-dependent* tensor via batched matrix multiplications. Given the center tensor $c_j \in \mathbb{R}^{m \times K}$ for column j , we evaluate candidate quantization levels $q_j \in \mathcal{Q}_j$ by broadcasting and compute the incremental costs $\Delta_j = R_{j,j}^2 |q_j - c_j|^2 \in \mathbb{R}^{m \times K \times A}$. We then update scores $S' = S + \Delta_j$ (broadcast over A), flatten the beam-and-choice axis, and keep the best K per row via `topk`, letting us update Q_{tail} . This implements an exact K -best search under the triangular branch metrics while remaining GPU-friendly. Algorithm 3 shows the K -SNRQ algorithm with lazy-batch update, and the dimension of matrices used is presented in Table 5.

For clarity, we define the three auxiliary operators used in Algorithm 3. All of them operate *row-wise* (independently for each output row $r \in [m]$), since the proxy objective decomposes over rows, as shown in Eq. (15).

TOPK(\mathbf{U}, K). Let $\mathbf{U} \in \mathbb{R}^{m \times K \times A}$ be a tensor of candidate costs, where K indexes the current beam and A indexes the discrete quantization levels. For each row r , define the set of all beam-level pairs $\Omega = \{(b, a) : b \in [K], a \in [A]\}$ and the corresponding costs $u_r(b, a) := \mathbf{U}_{r,b,a}$. TOPK returns the K smallest costs and their argmin indices:

$$\{(b_{r,k}^*, a_{r,k}^*)\}_{k=1}^K = \text{KSmallest}(\{u_r(b, a) : (b, a) \in \Omega\}, K),$$

and outputs

$$\mathbf{S}_{r,k} \leftarrow \mathbf{U}_{r,b_{r,k}^*,a_{r,k}^*}, \quad \mathbf{parent}_{r,k} \leftarrow b_{r,k}^*, \quad \mathbf{choice}_{r,k} \leftarrow a_{r,k}^*.$$

Intuitively, at each level we expand every current beam by all A levels, and keep the best K expansions per row.

GATHER($\mathbf{Z}, \mathbf{parent}$). This is the *beam reindexing* operator: it reorders a beam-dependent state tensor so that each surviving beam k inherits the state of its selected parent beam $\mathbf{parent}_{r,k}$. Formally, if $\mathbf{Z} \in \mathbb{R}^{m \times K \times d}$ (or any trailing shape d),

$$(\text{GATHER}(\mathbf{Z}, \mathbf{parent}))_{r,k,:} = \mathbf{Z}_{r,\mathbf{parent}_{r,k},:}, \quad \forall r \in [m], k \in [K].$$

We apply this to \mathbf{Q}_{blk} and \mathbf{T} (and to the ancestry map π) so that their beam dimension stays consistent with the pruned score tensor \mathbf{S} .

Algorithm 3 K -SNRQ: Beam Search Rounding with Lazy-Batch Update

Input: FP weight $\mathbf{W} \in \mathbb{R}^{m \times n}$, α -weighted input \mathbf{X}_α , student input \mathbf{X}_q , permutation \mathbf{P} , block size B , beam width K

Output: Quantized weight \mathbf{Q}

```

29  $\mathbf{H} \leftarrow (\mathbf{X}_q \mathbf{X}_q^\top + \lambda \mathbf{I})$ ,  $\mathbf{C}_\alpha = \mathbf{X}_\alpha \mathbf{X}_q^\top$ 
30  $\mathbf{H} \leftarrow \mathbf{P}^\top \mathbf{H} \mathbf{P}$ ,  $\mathbf{C}_\alpha \leftarrow \mathbf{P}^\top \mathbf{C}_\alpha \mathbf{P}$ 
31  $\mathbf{L} \leftarrow \text{CHOLESKY}(\mathbf{H})$ 
32  $\mathbf{L} \leftarrow \mathbf{L}/\text{diag}(\mathbf{L}) - \mathbf{I}$ 
33  $\mathbf{W} \leftarrow \mathbf{W} \mathbf{P}$ ,  $\mathbf{M}_\alpha \leftarrow \mathbf{W} \mathbf{C}_\alpha \mathbf{H}^{-1}$  // (permuted) shifted target
34 Initialize beam:  $\mathbf{S} \in \mathbb{R}^{m \times K} \leftarrow +\infty$ ,  $\mathbf{S}_{:,0} \leftarrow 0$  // beam scores (per row)
35  $\mathbf{Q}_{\text{tail}} \in \mathbb{R}^{m \times K \times 0} \leftarrow \emptyset$  // stored suffix decisions for each beam
36 for  $i = n, n - B, n - 2B, \dots$  do
37    $\mathbf{T} \leftarrow (\mathbf{M}_\alpha[:, i:] - \mathbf{Q}_{\text{tail}}) \mathbf{L}[i :, i-B : i] \in \mathbb{R}^{m \times K \times c}$ 
38    $\mathbf{Q}_{\text{blk}} \in \mathbb{R}^{m \times K \times c} \leftarrow \mathbf{0}$ ,  $\pi \in \mathbb{R}^{m \times K} \leftarrow [1, 2, \dots, K]$ 
39   for  $j = B - 1, B - 2, \dots, 0$  do
40      $t \leftarrow i - B + j$ 
41      $\tilde{\mathbf{W}} \leftarrow \mathbf{M}_\alpha[:, t] + (\mathbf{M}_\alpha[:, i-B : i] - \mathbf{Q}_{\text{blk}}[:, :, i-B : i]) \mathbf{L}[i-B : i, t] + \mathbf{T}[:, :, j] \in \mathbb{R}^{m \times K}$ 
42      $\mathbf{V} \leftarrow \text{LEVELS}(\tilde{\mathbf{W}}) \in \mathbb{R}^{m \times A}$ 
43      $\Delta \leftarrow \mathbf{L}[t : t]^2 |\tilde{\mathbf{W}} - \mathbf{V}|^2 \in \mathbb{R}^{m \times K \times A}$ 
44      $(\mathbf{S}, \mathbf{parent}, \mathbf{choice}) \leftarrow \text{TOPK}(\mathbf{S} + \Delta, K)$  // keep best  $K$  over  $B \times A$ 
45      $\mathbf{Q}_{\text{blk}} \leftarrow \text{GATHER}(\mathbf{Q}_{\text{blk}}, \mathbf{parent})$ 
46      $\mathbf{T} \leftarrow \text{GATHER}(\mathbf{T}, \mathbf{parent})$ 
47      $\pi \leftarrow \text{GATHER}(\pi, \mathbf{parent})$ 
48      $\mathbf{Q}_{\text{blk}}[:, :, j] \leftarrow \text{PICKLEVEL}(\mathbf{V}, \mathbf{choice})$  // selected level for column  $t$ 
49   end
50    $\mathbf{Q}_{\text{tail}} \leftarrow \text{Concat}(\mathbf{Q}_{\text{blk}}, \text{GATHER}(\mathbf{Q}_{\text{tail}}, \pi))$ 
51 end
52  $k_r^* \leftarrow \arg \min_{k \in [K]} \mathbf{S}_{r,k}$ ,  $\forall r \in [m]$  // best beam per row
53  $\mathbf{Q}_p[r, :] \leftarrow \mathbf{Q}_{\text{tail}}[r, k_r^*, :], \forall r \in [m]$ 
54  $\mathbf{Q} \leftarrow \mathbf{Q}_p \mathbf{P}^\top$  // undo permutation
55 return  $\mathbf{Q}$ 

```

PICKLEVEL(\mathbf{V} , \mathbf{choice}). Given candidate quantization values $\mathbf{V} \in \mathbb{R}^{m \times A}$ for the current column and selected level indices $\mathbf{choice} \in \mathbb{R}^{m \times K}$, PICKLEVEL returns the chosen quantized values per row/beam:

$$(\text{PICKLEVEL}(\mathbf{V}, \mathbf{choice}))_{r,k} = \mathbf{V}_{r, \mathbf{choice}_{r,k}}, \quad \forall r \in [m], k \in [K].$$

This is exactly the column update $\mathbf{Q}_{\text{blk}}[:, :, j]$ for the surviving beams.

In implementation, TOPK corresponds to a row-wise `topk` on the flattened beam-level axis, while GATHER and PICKLEVEL are indexed gathers along the beam and level dimensions, respectively.

B. Theoretical Results

B.1. Asymmetric Loss as Regularization

Proposition B.1 (Decomposition of the regularized calibration proxy). *For any $\alpha \in [0, 1]$, the regularized proxy $\mathcal{L}(\hat{W}; \alpha)$ admits the decomposition*

$$\mathcal{L}(\hat{W}; \alpha) \equiv \alpha \mathcal{L}_{\text{asym}}(\hat{W}) + (1 - \alpha) \mathcal{L}_{\text{sym}}(\hat{W}), \quad (27)$$

where \equiv denotes equality up to an additive constant independent of \hat{W} . In particular,

$$\mathcal{L}(\hat{W}; \alpha) = \alpha \mathcal{L}_{\text{asym}}(\hat{W}) + (1 - \alpha) \mathcal{L}_{\text{sym}}(\hat{W}) - \alpha(1 - \alpha) \|W(X_f - X_q)\|_F^2. \quad (28)$$

Proof.

$$WX_\alpha - \hat{W}X_q = W(\alpha X_f + (1 - \alpha)X_q) - \hat{W}X_q \quad (29)$$

$$= \alpha(WX_f - \hat{W}X_q) + (1 - \alpha)(WX_q - \hat{W}X_q). \quad (30)$$

Define $A := WX_f - \hat{W}X_q$, and $B := WX_q - \hat{W}X_q$. Then $WX_\alpha - \hat{W}X_q = \alpha A + (1 - \alpha)B$ and thus

$$\|WX_\alpha - \hat{W}X_q\|_F^2 = \|\alpha A + (1 - \alpha)B\|_F^2. \quad (31)$$

Using the standard squared-norm identity (valid for Frobenius norms),

$$\|\alpha A + (1 - \alpha)B\|_F^2 = \alpha\|A\|_F^2 + (1 - \alpha)\|B\|_F^2 - \alpha(1 - \alpha)\|A - B\|_F^2, \quad (32)$$

we obtain

$$\|WX_\alpha - \hat{W}X_q\|_F^2 = \alpha\|A\|_F^2 + (1 - \alpha)\|B\|_F^2 - \alpha(1 - \alpha)\|A - B\|_F^2. \quad (33)$$

The first two terms are exactly $\alpha \mathcal{L}_{\text{asym}}(\hat{W})$ and $(1 - \alpha) \mathcal{L}_{\text{sym}}(\hat{W})$. Finally,

$$A - B = (WX_f - \hat{W}X_q) - (WX_q - \hat{W}X_q) = W(X_f - X_q),$$

which does not depend on \hat{W} and yields (28). \square

B.2. Joint optimization over \hat{W} and the interpolation coefficient α

We derive the closed-form update of α in SNRQ-C in this subsection. Recall the α -blended input activation

$$X_\alpha = \alpha X_f + (1 - \alpha)X_q = X_q + \alpha(X_f - X_q),$$

and the interpolated proxy objective

$$\mathcal{L}(\hat{W}; \alpha) = \|WX_\alpha - \hat{W}X_q\|_F^2.$$

Feasible set for quantization. Let \mathcal{Q} denote the feasible set of quantized weights (e.g., per-group uniform quantization grids, with fixed bit-width, scale, and zero-point). We consider the joint optimization problem

$$\min_{\hat{W} \in \mathcal{Q}, \alpha \in [0, 1]} \mathcal{L}(\hat{W}, \alpha) := \|WX_\alpha - \hat{W}X_q\|_F^2. \quad (34)$$

A useful reparameterization. Define the feature mismatch and its image under the teacher:

$$\Delta X := X_f - X_q \in \mathbb{R}^{n \times N}, \quad U := W\Delta X \in \mathbb{R}^{m \times N}.$$

Also define the “symmetric residual” induced by \hat{W} on quantized features:

$$V(\hat{W}) := (W - \hat{W})X_q \in \mathbb{R}^{m \times N}.$$

Then the joint objective can be written as

$$\begin{aligned} WX_\alpha - \hat{W}X_q &= W(X_q + \alpha\Delta X) - \hat{W}X_q \\ &= (W - \hat{W})X_q + \alpha W\Delta X \\ &= V(\hat{W}) + \alpha U, \end{aligned} \quad (35)$$

hence

$$\mathcal{L}(\hat{W}, \alpha) = \|V(\hat{W}) + \alpha U\|_F^2. \quad (36)$$

B.2.1. CLOSED-FORM OPTIMAL α FOR FIXED \hat{W}

For any fixed $\hat{W} \in \mathcal{Q}$, (36) is a convex quadratic in α :

$$\mathcal{L}(\hat{W}, \alpha) = \left(\|V(\hat{W})\|_F^2 + 2\alpha\langle V(\hat{W}), U \rangle_F + \alpha^2\|U\|_F^2 \right), \quad (37)$$

where $\langle A, B \rangle_F := \text{tr}(A^\top B)$.

Proposition B.2 (Optimal α). *Fix any $\hat{W} \in \mathcal{Q}$. If $U \neq 0$, then the unique minimizer of $\alpha \mapsto \mathcal{L}(\hat{W}, \alpha)$ over $[0, 1]$ is*

$$\alpha^*(\hat{W}) = \Pi_{[0,1]} \left(-\frac{\langle (W - \hat{W})X_q, W(X_f - X_q) \rangle_F}{\|W(X_f - X_q)\|_F^2} \right), \quad (38)$$

where $\Pi_{[0,1]}(t) := \min\{1, \max\{0, t\}\}$ is the Euclidean projection onto $[0, 1]$. If $U = 0$ (equivalently $W(X_f - X_q) = 0$), then $\mathcal{J}(\hat{W}, \alpha)$ does not depend on α and any $\alpha \in [0, 1]$ is optimal.

Proof. Assume $U \neq 0$. Differentiating (37) gives

$$\frac{\partial}{\partial \alpha} \mathcal{L}(\hat{W}, \alpha) = 2\left(\langle V(\hat{W}), U \rangle_F + \alpha\|U\|_F^2\right).$$

The unconstrained minimizer is

$$\alpha_0(\hat{W}) = -\frac{\langle V(\hat{W}), U \rangle_F}{\|U\|_F^2}.$$

Since $\mathcal{J}(\hat{W}, \alpha)$ is convex in α , the constrained minimizer over $[0, 1]$ is obtained by projecting $\alpha_0(\hat{W})$ onto the interval:

$$\alpha^*(\hat{W}) = \Pi_{[0,1]}(\alpha_0(\hat{W})),$$

which is exactly (38) after substituting $V(\hat{W}) = (W - \hat{W})X_q$ and $U = W(X_f - X_q)$. If $U = 0$, then (36) reduces to $\mathcal{L}(\hat{W}, \alpha) = \frac{1}{N}\|V(\hat{W})\|_F^2$, independent of α . \square

B.3. Sampling α for robust calibration in SNRQ-S

The empirical benefits of sampling α in SNRQ-S are primarily observed as reduced run-to-run variability in low-bit quantization (Fig. 3). However, since our PTQ pipeline applies a discrete rounding $M \mapsto Q(M)$, it is generally difficult to give deterministic guarantees that sampling improves the realized quantization error for every calibration set. Instead, we formalize a simple but principled statement: sampling α can be viewed as injecting a controlled, zero-mean perturbation into the shifted target prior to rounding, which smooths boundary effects of the discrete rounding rule. Under a simple probabilistic model for calibration-set fluctuations and this injected perturbation, the resulting smoothing yields an explicit reduction in calibration-induced variability.

Concretely, let S denote the calibration set and let $M_\mu(S)$ be the shifted target computed with a fixed interpolation $\alpha = \mu := \mathbb{E}[\alpha]$. Under sequence-wise sampling α_j , the sampled cross-moment satisfies

$$C_\alpha(S) = H + \sum_{j=1}^N \alpha_j D_j(S) = C_\mu(S) + \sum_{j=1}^N (\alpha_j - \mu) D_j(S), \quad D_j(S) := \Delta X^{(j)} X_q^{(j)\top},$$

and therefore the sampled shifted target can be written as

$$M_\alpha(S) = WC_\alpha(S)H^{-1} = M_\mu(S) + Z(S), \quad Z(S) := W \left(\sum_{j=1}^N (\alpha_j - \mu) D_j(S) \right) H^{-1}. \quad (39)$$

Thus $Z(S)$ is a sum of independent, zero-mean scalar coefficients $(\alpha_j - \mu)$ modulating per-sequence matrices $D_j(S)$, and it acts as a “dither” on the target presented to the rounding map. When N is moderately large, such sums are well-approximated by a Gaussian distribution along any fixed projection by the central limit theorem, motivating the Gaussian assumption for Z in the proposition below.

The proposition then shows, in a one-dimensional setting where the fixed- α target concentrates near a rounding boundary, that deterministic rounding can exhibit non-vanishing calibration variance, whereas dithering yields an $O(1/N)$ variance bound for a smoothed metric. This provides a concrete mechanism by which sampling can reduce sensitivity to calibration-set fluctuations in low-bit regimes.

Proposition B.3 (Calibration-set variance under Gaussian dithering for binary rounding). *Consider scalar rounding on the binary grid $\mathcal{Q} = \{0, 1\}$ with decision rule $Q(m) = \mathbf{1}\{m \geq \frac{1}{2}\}$. Let $W = w \in \mathbb{R}$ and $X = x \in \mathbb{R}$ be fixed scalars, and define the activation error metric*

$$\ell(Q) = \|(Q - w)x\| = |x| \cdot |Q - w|.$$

Assume the fixed-mean target induced by a random calibration set S satisfies $M_\mu(S) = \frac{1}{2} + U$, $U \sim \mathcal{N}\left(0, \frac{\tau_S^2}{N}\right)$, and that a stochastic interpolation rule induces an additive perturbation (dither) $M_\alpha(S) = M_\mu(S) + Z$, $Z \sim \mathcal{N}(0, \tau_Z^2)$, where Z is independent of U . Define the fixed- μ output $Q_{\text{fix}}(S) := Q(M_\mu(S))$, and the smoothed conditional metric

$$G(S) := \mathbb{E}_Z [\ell(Q(M_\mu(S) + Z)) \mid S].$$

Then we have

$$\text{Var}_S(\ell(Q_{\text{fix}}(S))) = \frac{|x|^2}{4} \left(|1 - w| - |w| \right)^2.$$

In particular, if $|1 - w| \neq |w|$, this variance is strictly positive and does not decay with N .

The smoothed metric admits a closed form

$$G(S) = |x| \left(|w| + (|1 - w| - |w|) \Phi(U/\tau_Z) \right),$$

and satisfies the variance bound

$$\text{Var}_S(G(S)) \leq \frac{|x|^2 (|1 - w| - |w|)^2}{2\pi \tau_Z^2} \cdot \frac{\tau_S^2}{N} = O\left(\frac{1}{N}\right),$$

where Φ is the standard normal CDF.

Proof. Since $Q_{\text{fix}}(S) = \mathbf{1}\{U \geq 0\}$ and U is symmetric, we have $\mathbb{P}(Q_{\text{fix}} = 1) = \mathbb{P}(Q_{\text{fix}} = 0) = 1/2$ for all N . Hence

$$\ell(Q_{\text{fix}}(S)) = |x| \cdot \begin{cases} |1 - w|, & U \geq 0, \\ |w|, & U < 0, \end{cases}$$

which yields

$$\text{Var}_S(\ell(Q_{\text{fix}}(S))) = \frac{1}{2} (|x| |1 - w|)^2 + \frac{1}{2} (|x| |w|)^2 - \left(\frac{|x| |1 - w| + |x| |w|}{2} \right)^2 = \frac{|x|^2}{4} (|1 - w| - |w|)^2.$$

Next, conditioned on U , we have $Q(M_\mu(S) + Z) = \mathbf{1}\{U + Z \geq 0\}$, so

$$p(U) := \mathbb{P}(Q = 1 \mid U) = \mathbb{P}(Z \geq -U) = \Phi(U/\tau_Z).$$

Therefore

$$G(S) = |x| \left(|w| \cdot (1 - p(U)) + |1 - w| \cdot p(U) \right) = |x| \left(|w| + (|1 - w| - |w|) \Phi(U/\tau_Z) \right).$$

Since $\Phi'(t) = \phi(t)$ and $\phi(t) = (2\pi)^{-1/2} e^{-t^2/2} \leq \phi(0) = 1/\sqrt{2\pi}$, we have

$$\left| \frac{d}{dU} G(S) \right| = |x| \cdot ||1 - w| - |w|| \cdot \frac{1}{\tau_Z} \phi(U/\tau_Z) \leq \frac{|x| ||1 - w| - |w||}{\sqrt{2\pi} \tau_Z} =: L.$$

Hence $G(S) = g(U)$ is L -Lipschitz in U , so $\text{Var}(g(U)) \leq L^2 \text{Var}(U)$. Using $\text{Var}(U) = \tau_S^2/N$ gives the stated bound. \square

B.4. Difference in the objectives of SNRQ and GPTAQ

GPTAQ (Li et al., 2025) targets $\|WX_f - \hat{W}X_q\|_F^2$ and uses an iterative approximation to the mismatch residual to avoid recomputing $W(X_f - X_q)$ during columnwise updates. Our objective and solver instead reduce the asymmetric proxy to the shifted target matrix M_α , so the mismatch enters through the closed-form cross-moment C_α and does not require repeated residual recomputation as stated in Theorem 4.1. Here, we provide a detailed comparison.

Let $W \in \mathbb{R}^{m \times n}$ be the full-precision weight matrix. Let $X_f, X_q \in \mathbb{R}^{n \times N}$ denote the full-precision and quantized inputs (activations) used in calibration, and define

$$X := X_q, \quad \Delta X := X_f - X_q.$$

Let the quantized weight be \hat{W} , and define $\Delta W := \hat{W} - W$. Consider the asymmetric proxy loss ($\alpha = 1$ case):

$$\mathcal{L}(\Delta W) := \|\Delta W X - W \Delta X\|_F^2. \quad (40)$$

Define the residual

$$R := W \Delta X \in \mathbb{R}^{m \times N}.$$

Then $\mathcal{L}(\Delta W) = \|\Delta W X - R\|_F^2$.

GPTAQ optimization problem Partition columns/rows as

$$\Delta W = [\Delta W_{:, < q} \ \Delta W_{:, q:}], \quad X = \begin{bmatrix} X_{< q, :} \\ X_{q:, :} \end{bmatrix},$$

where “ $< q$ ” means indices $1, \dots, q-1$ and “ $q :$ ” means q, \dots, n . At step q , the first $q-1$ columns are already fixed (quantized), so $\Delta W_{:, < q}$ is treated as constant and the optimization variable is the whole tail block $\Delta W_{:, q:}$. Thus the exact minimization for (40) is

$$\min_{\Delta W_{:, q:}} \|\Delta W_{:, q:} X_{q:, :} - T_q\|_F^2 \quad \text{s.t.} \quad W_{:, q} + \Delta W_{:, q} = \hat{W}_{:, q}, \quad (41)$$

where the (step-dependent) target is

$$T_q := R - \Delta W_{:, < q} X_{< q, :}. \quad (42)$$

Note that T_q depends on the already-fixed earlier columns through $\Delta W_{:, < q}$. To avoid repeated computation of T_q , GPTAQ uses the identity

$$R = W \Delta X = \sum_{k=1}^n W_{:, k} \Delta X_{k, :} \quad (43)$$

and replaces the full target T_q by the *single-component* term

$$r_q := W_{:, q} \Delta X_{q, :},$$

and solves the surrogate tail problem

$$\min_{\Delta W_{:, q:}} \|\Delta W_{:, q:} X_{q:, :} - r_q\|_F^2 \quad \text{s.t.} \quad W_{:, q} + \Delta W_{:, q} = \hat{W}_{:, q}. \quad (44)$$

Are Eq. (41) and Eq. (44) equivalent?

Proposition B.4. Define the “omitted” term

$$C_q := T_q - r_q = \left(R - \Delta W_{:, < q} X_{< q, :} \right) - W_{:, q} \Delta X_{q, :} \quad (45)$$

Let $A(\Delta W_{:, q:}) := \Delta W_{:, q:} X_{q, :}$. Then the exact objective in (41) equals

$$f(\Delta W_{:, q:}) := \|A(\Delta W_{:, q:}) - (r_q + C_q)\|_F^2,$$

while the GPTAQ surrogate objective in (44) equals

$$g(\Delta W_{:, q:}) := \|A(\Delta W_{:, q:}) - r_q\|_F^2.$$

Moreover,

$$f(\Delta W_{:, q:}) = g(\Delta W_{:, q:}) - 2\langle A(\Delta W_{:, q:}) - r_q, C_q \rangle_F + \|C_q\|_F^2, \quad (46)$$

and the difference $f - g$ is constant in $\Delta W_{:, q:}$ if and only if $C_q X_{q, :}^\top = 0$.

Proof. Starting from $f(\Delta W_{:, q:}) = \|A - r_q - C_q\|_F^2$ and expanding the square gives (46).

It remains to characterize when the middle (cross) term depends on $\Delta W_{:, q:}$. Using the Frobenius inner product identity $\langle UX, C \rangle_F = \langle U, CX^\top \rangle_F$ (valid for compatible matrices), we have

$$\langle A(\Delta W_{:, q:}), C_q \rangle_F = \langle \Delta W_{:, q:} X_{q, :}, C_q \rangle_F = \langle \Delta W_{:, q:}, C_q X_{q, :}^\top \rangle_F.$$

Hence $\langle A(\Delta W_{:, q:}), C_q \rangle_F$ is constant in $\Delta W_{:, q:}$ for all feasible $\Delta W_{:, q:}$ if and only if $C_q X_{q, :}^\top = 0$. \square

Remarks. Because the tail minimization (error feedback) solution to a least-squares problem depends on the target through correlations with $X_{q, :}$, replacing T_q by r_q changes the continuous optimum $\Delta W_{:, q:}^*$ in general, and therefore can change the discrete greedy choice for the quantized column $\hat{W}_{:, q}$ as well. If GPTAQ did *not* apply the surrogate replacement $T_q \mapsto r_q$ and instead solved the exact problem (41) (i.e., it used the original residual target T_q), it would yield equivalent solution to SNRQ’s solution provided by the equivalence between GPTQ and LDLQ (Theorem 6 of (Chee et al., 2023))

C. Experimental Results

C.1. Ablation Study

C.1.1. DIFFERENT CHOICE OF λ

We ablate the sampling parameter λ in SNRQ-S by sweeping $\lambda \in \{1, 2, 5, 10, 20\}$. For L2-7B and L2-13B, perplexity varies only mildly across the sweep, indicating that the method is robust to λ in typical regimes. For L3-8B, smaller λ can be less favorable on Wiki2, while moderate values yield the best results. Conceptually, λ controls how aggressively the sampled interpolation emphasizes one side of the objective; moderate values avoid over-committing to extreme and thus provide a reliable default. Overall, SNRQ-S does not require fine-grained tuning of λ , and that intermediate values offer consistently strong performance across models and datasets.

C.1.2. EFFECT OF CALIBRATION AND ROUNDING

Table 6 presents an ablation of search strategies under the symmetric calibration (SNQ) and our regularized calibration (SNRQ-S). Holding the calibration procedure fixed, we vary the beam width K to isolate the effect of discrete search. For SNQ, beam search consistently improves perplexity over greedy rounding, confirming the benefit of search under a symmetric objective. In contrast, SNRQ-S already performs well with greedy rounding, and beam search yields additional gains at larger beam widths. This shows that asymmetric calibration reduces rounding ambiguity, while search further improves performance by resolving remaining discrete uncertainty.

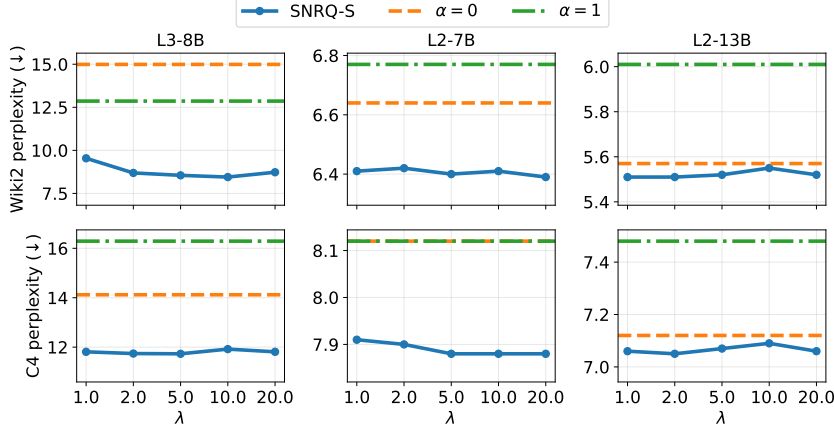

 Figure 7. Robustness to sampling parameter λ in SNRQ-S.

 Table 6. Ablation of search strategies on symmetric (SNQ) v.s. our objective with sampling α (SNRQ-S).

Objective	Beam size	Wiki2 (\downarrow)	C4 (\downarrow)	Q.Time (s) \downarrow
K -SNQ	$K = 1$	6.635 ± 0.057	8.119 ± 0.019	427.8
	$K = 2$	6.511 ± 0.014	8.045 ± 0.010	579.0
	$K = 4$	6.523 ± 0.016	8.044 ± 0.018	591.0
	$K = 6$	6.473 ± 0.022	8.024 ± 0.012	602.1
K -SNRQ	$K = 1$	6.411 ± 0.026	7.884 ± 0.012	449.0
	$K = 2$	6.427 ± 0.196	7.847 ± 0.016	586.5
	$K = 4$	6.350 ± 0.037	7.839 ± 0.013	589.2
	$K = 6$	6.328 ± 0.035	7.835 ± 0.011	618.7

C.2. Limitation of Pure Asymmetric Calibration

Does larger α reduce the teacher–student mismatch? A natural hypothesis is that increasing α —placing more weight on teacher-side features—should reduce the mismatch between X_f and X_q . On the calibration set, this trend indeed holds: larger α produces smaller deviation, as expected. However, this behavior does not reliably transfer to held-out data. On the validation set, increasing α can *increase* the deviation between X_f and X_q , indicating that aggressive teacher-side matching may overfit to calibration-specific mismatch patterns and hurt generalization.

This effect is reflected in end-to-end quantization performance. As shown in Table 7, L2-7B and L3-8B achieve their best overall results at an intermediate value (around $\alpha = 0.5$), consistent with the validation MAE trends: moderate asymmetry improves generalization, whereas $\alpha = 1$ (pure asymmetric calibration) leads to notable degradation, especially for L3-8B. For L2-13B, the validation MAE curves are nearly indistinguishable across α , and the corresponding quantization results exhibit a weaker sensitivity to α , suggesting that the optimal asymmetry level can be model-dependent and may diminish as the model becomes more robust to prefix mismatch.

 Table 7. 3-bit quantization results on different fixed α values (used random seed 0, matching with Fig. 8)

α	L2-7B			L2-13B			L3-8B		
	Wiki2 (\downarrow)	C4 (\downarrow)	Avg.Acc (\uparrow)	Wiki2 (\downarrow)	C4 (\downarrow)	Avg.Acc (\uparrow)	Wiki2 (\downarrow)	C4 (\downarrow)	Avg.Acc (\uparrow)
0.0	6.62	8.13	66.48	5.53	7.13	71.14	12.85	13.33	65.78
0.25	6.38	7.89	66.93	5.56	7.12	70.33	9.49	11.96	69.53
0.5	6.37	7.86	66.96	5.62	7.16	70.73	8.48	11.87	70.53
0.75	6.43	7.96	66.87	5.79	7.29	69.30	8.94	12.65	68.26
1.0	6.52	8.05	66.55	5.72	7.23	70.45	11.98	15.48	55.52

C.3. Additional Results

C.3.1. L2-70B PER-GROUP QUANTIZATION

We evaluate SNRQ on the 70B-scale LLaMA2 model using per-group weight-only quantization. While quantizing L2-70B is substantially more expensive than smaller models due to its size and memory traffic, Table 8 shows that SNRQ remains

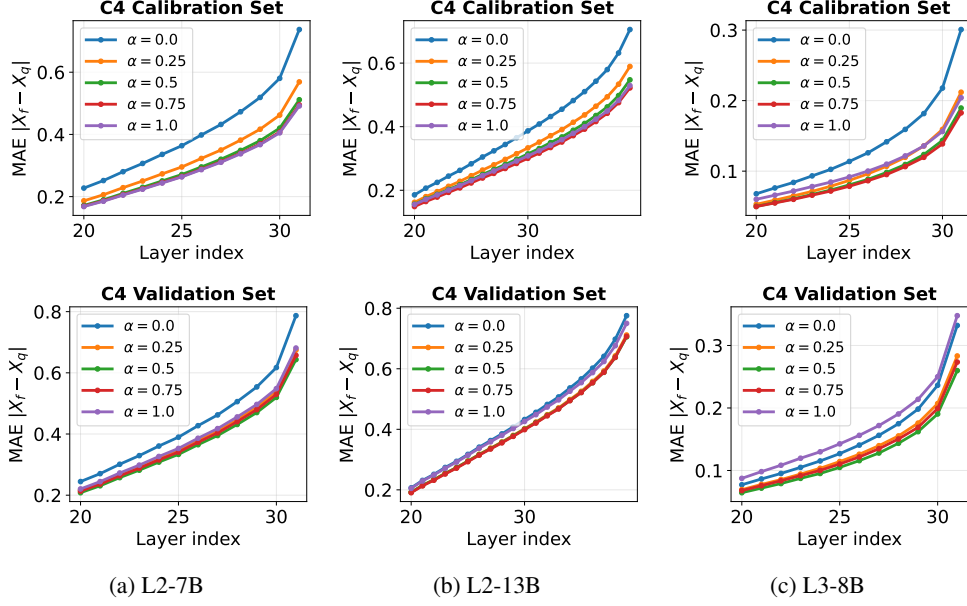


Figure 8. Mean activation error (MAE) measured on (top) calibration and (bottom) validation set.

competitive with strong Hessian-based baselines. In particular, under 3-bit quantization, SNRQ-S achieves the best perplexity on both Wiki and C4, and under 4-bit quantization both SNRQ variants match or slightly improve upon GPTQ/LDLQ while maintaining comparable quantization time. These results suggest that the proposed objective and rounding strategy scale to large models without sacrificing efficiency.

Table 8. 3-bit per-group symmetric quantization on L2-70B.

Model	bits	Method	Wiki (\downarrow)	C4 (\downarrow)	Q.Time (s)
L2-70B	3	FP16	3.32	5.52	
		GPTQ	4.00	5.95	3381.6
		GPTAQ	4.01	5.95	4762.2
		LDLQ	4.00	5.96	3416.0
		SNRQ-C	4.01	5.95	4026.5
		SNRQ-S	3.99	5.94	3899.8
	4	GPTQ	3.45	5.60	3382.3
		GPTAQ	3.47	5.62	4835.4
		LDLQ	3.45	5.60	3582.1
		SNRQ-C	3.44	5.59	3893.7
		SNRQ-S	3.44	5.60	3713.2

C.3.2. RESULTS WITH OUTLIER REDUCTION: RANDOM HADAMARD TRANSFORM

Table 9 evaluates quantization results with random Hadamard transforms (RHT) following (Chee et al., 2023; Tseng et al., 2024). Across methods, RHT consistently improves perplexity. When combined with SNRQ, RHT delivers the strongest overall performance. For instance, on L3-8B, SNRQ-S+RHT improves over SNRQ-S by about 5% on Wiki2 and 3% on C4, and it improves over GPTAQ+RHT by about 3% on both Wiki2 and C4 while also increasing accuracy by about 1.5%. Overall, RHT is a complementary preprocessing step for SNRQ that yields consistent perplexity improvements with a moderate runtime overhead.

C.3.3. BEAM SEARCH IN THE 2-BIT REGIME

Table 10 evaluates beam search with random Hadamard transform (RHT) preprocessing for 2-bit symmetric weight-only quantization. Overall, beam search yields consistent improvements on C4, while the effect on Wiki2 is more nuanced. For L2-7B, increasing the beam width reduces both Wiki2 and C4 perplexity relative to greedy rounding, with the strongest gains observed on C4. For L2-13B, the Wiki2 results for beam widths $K=1-3$ largely overlap within the reported error

Table 9. 3-bit quantization results with incoherence processing (Chee et al., 2023; Tseng et al., 2024). We bold the best results, as well as those whose value falls within the top score \pm standard deviation.

Model	Method	Wiki2 (↓)	C4 (↓)	Avg.Acc (↑)	Q.Time (s)
L3-8B	QuIP	8.63	11.80	67.60	763.8
	GPTAQ	9.07	12.15	65.77	715.0
	SNRQ-C	8.74	11.87	67.60	594.4
	SNRQ-S	8.55	11.73	69.33	542.8
	GPTAQ+RHT	8.34	11.61	68.73	853.1
	SNRQ-C+RHT	8.27	11.58	69.01	741.8
	SNRQ-S+RHT	8.11	11.37	69.78	688.7
L2-7B	QuIP	6.47	8.02	66.22	704.8
	GPTAQ	6.57	8.04	66.34	590.4
	SNRQ-C	6.41	7.89	66.82	517.1
	SNRQ-S	6.40	7.88	67.34	449.0
	GPTAQ+RHT	6.32	7.86	67.02	795.7
	SNRQ-C+RHT	6.32	7.82	67.26	697.3
	SNRQ-S+RHT	6.28	7.77	67.18	644.5
L2-13B	QuIP	5.53	7.15	70.76	1096.2
	GPTAQ	5.54	7.10	71.00	1012.0
	SNRQ-C	5.57	7.10	71.06	965.0
	SNRQ-S	5.52	7.07	71.11	786.4
	GPTAQ+RHT	5.49	7.07	70.86	1259.4
	SNRQ-C+RHT	5.50	7.05	70.71	1106.3
	SNRQ-S+RHT	5.47	7.03	70.90	970.2

bars, whereas $K=4$ provides a clear improvement with lower mean perplexity; on C4, the gains are smaller but still trend favorably with larger beams. Although performance is not strictly monotonic in K —reflecting stochasticity and the locally ambiguous nature of low-bit rounding—the results demonstrate that beam search remains effective in challenging 2-bit regimes and continues to provide benefits even when combined with structured preprocessing such as RHT. In exchange, beam search increases peak GPU memory with K (as expected from maintaining more candidates), while search time grows moderately and remains comparable among $K > 1$ settings due to batching.

Table 10. 2-bit weight-only symmetric quantization with random Hadamard transform (RHT) on L2-7B. Search time and peak GPU memory usage are measured during search only, and we report the metric averaged over 32 layers.

Model	Search	Beam K	Wiki2 (↓)	C4 (↓)	Search Time (ms)	Peak Mem (GB)
L2-7B	Greedy	1	16.64 ± 0.39	15.43 ± 0.41	1036.3	17.06
	Beam	2	16.34 ± 0.82	15.22 ± 0.24	1854.3	18.38
	Beam	3	16.23 ± 0.37	15.20 ± 0.22	1822.5	18.78
	Beam	4	16.33 ± 1.03	15.21 ± 0.22	1863.0	19.17
L2-13B	Greedy	1	11.41 ± 0.45	11.84 ± 0.15	1268.1	21.68
	Beam	2	11.46 ± 0.48	11.86 ± 0.18	2447.7	23.75
	Beam	3	11.47 ± 0.50	11.83 ± 0.14	2312.2	24.42
	Beam	4	11.21 ± 0.25	11.78 ± 0.17	2402.6	25.10

C.3.4. QUANTIZATION RESULTS OF VISION TRANSFORMERS

Table 11 reports W2A4 post-training quantization results for vision transformers, including DeiT-S and DeiT-B (Touvron et al., 2021) with 22M and 86M parameters, respectively. We follow the experimental protocol of Li et al. (2025): 128 images are sampled from the ImageNet training set and used for calibration. We apply weight clipping based on mean squared error and adopt asymmetric quantization grids for both weights and activations. Quantization time is measured on a single NVIDIA RTX 6000 Ada Generation GPU.

It shows that SNRQ and K -SNRQ improve over GPTAQ in terms of downstream ImageNet accuracy. Since ImageNet accuracy does not depend linearly on the layer-wise calibration objective, the accuracy does not increase monotonically with the beam size K . Nevertheless, small beams ($K = 2$ or 3) already yield consistent gains with a moderate increase in quantization time, while remaining comparable to GPTAQ in overall runtime.

Table 11. W2A4 quantization results of vision transformers. We use a unified $\lambda = 0.1$ for SNRQ-S. All results are averaged over 5 random seeds.

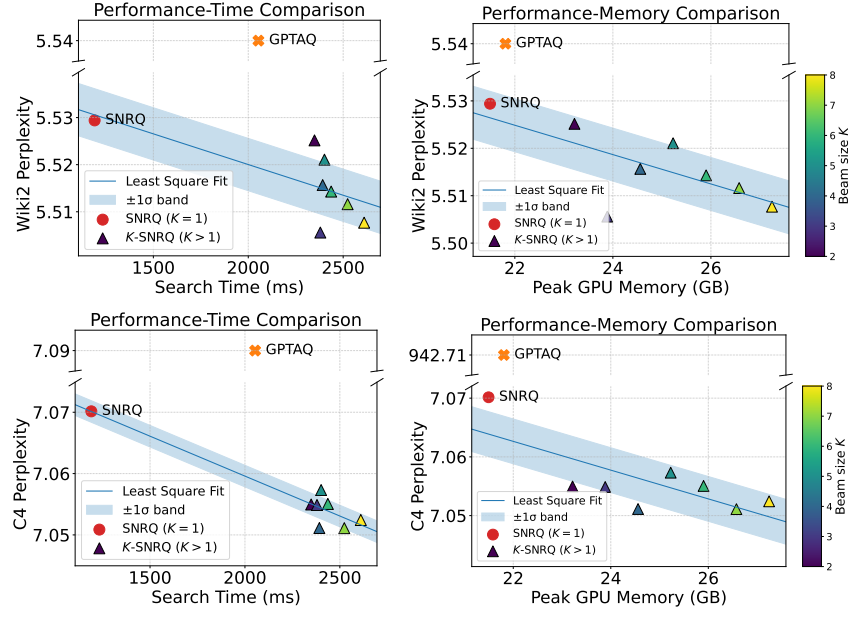
Method	K	DeiT-S		DeiT-B	
		Acc (%)	Q.Time (s)	Acc (%)	Q.Time (s)
FP16	–	79.9	–	81.8	–
GPTQ	–	44.49	14.97	61.82	21.70
GPTAQ	–	45.57	18.61	61.47	28.98
SNRQ	1	46.58	16.92	62.64	24.81
K -SNRQ	2	47.00	18.70	62.80	30.07
	3	46.84	19.12	63.09	29.36
	4	46.61	18.95	63.19	29.47

Table 12. Average extra GPU time (ms) per module in L2-7B from (i) obtaining closed-form α in SNRQ-C and (ii) sampling in SNRQ-S.

Method	attn.k-proj	attn.v-proj	attn.q-proj	attn.o-proj	mlp.up-proj	mlp.gate-proj	mlp.down-proj	Avg
SNRQ-C	17.22	10.46	10.46	10.32	27.07	27.02	85.21	26.82
SNRQ-S	10.04	0	0	9.99	10.15	0	36.75	16.73

Table 13. Beam width vs. coordinate-descent (CD) passes (Chee et al., 2023): perplexity–time–memory trade-off.

Beam K	CD pass	Wiki2 (\downarrow)	C4 (\downarrow)	Search Time (ms)	Peak Mem (GB)
1	0	6.41	7.88	935.05	16.95
	1	6.37	7.87	2228.57	17.20
	2	6.38	7.87	3677.29	17.20
	3	6.38	7.86	5031.12	17.20
2	0	6.43	7.85	1776.20	18.04
	1	6.36	7.84	3029.62	18.18
	2	6.34	7.83	4430.68	18.18
	3	6.37	7.84	5647.55	18.18
4	0	6.36	7.84	7025.00	18.18
	1	6.35	7.84	1782.96	18.90
	2	6.34	7.83	3184.99	18.90
	3	6.33	7.82	4537.75	18.89
6	0	6.33	7.83	5857.70	18.89
	1	6.40	7.83	7190.50	18.89
	2	6.35	7.83	1887.06	19.74
	3	6.34	7.82	3246.22	19.75
8	0	6.34	7.82	4614.72	19.75
	1	6.34	7.82	5979.73	19.75
	2	6.34	7.82	7132.99	19.76



(a) Performance-Time

(b) Performance-Memory

Figure 9. Performance–efficiency trade-offs of beam search for 3-bit quantized L2-13B. Wiki2 (top) and C4 (bottom) perplexity are shown as functions of quantization time (left) and peak GPU memory (right).